

**YAŞAR UNIVERSITY
GRADUATE SCHOOL OF NATURAL AND APPLIED SCIENCES**

PhD THESIS

**ESTIMATING MISSING BRDF MEASUREMENTS
WITH COMPRESSED SAMPLING METHOD**

Nurcan SEYLAN

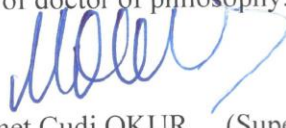
Thesis Advisor: Prof. Dr. Mehmet Cudi OKUR

Department of Computer Engineering

Presentation Date: 16.09.2015

**Bornova-İZMİR
2015**

I certify that I have read this thesis and that in my opinion it is fully adequate,
in scope and in quality, as a dissertation for the degree of doctor of philosophy.



Prof. Dr. Mehmet Cudi OKUR (Supervisor)

I certify that I have read this thesis and that in my opinion it is fully adequate,
in scope and in quality, as a dissertation for the degree of doctor of philosophy.



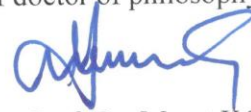
Prof. Dr. Aydın ÖZTÜRK

I certify that I have read this thesis and that in my opinion it is fully adequate,
in scope and in quality, as a dissertation for the degree of doctor of philosophy.



Assist. Prof. Dr. Korhan KARABULUT

I certify that I have read this thesis and that in my opinion it is fully adequate,
in scope and in quality, as a dissertation for the degree of doctor of philosophy.



Assoc. Prof. Dr. Murat KOMESLI

I certify that I have read this thesis and that in my opinion it is fully adequate,
in scope and in quality, as a dissertation for the degree of doctor of philosophy.



Assist. Prof. Dr. Cengiz GÜNGÖR



Prof. Dr. Behzat GÜRKAN
Director of the Graduate School

ABSTRACT

ESTIMATING MISSING BRDF MEASUREMENTS

WITH COMPRESSED SAMPLING METHOD

SEYLAN, Nurcan

PhD in Computer Engineering

Supervisor: Prof. Dr. Mehmet Cudi OKUR

September 2015, 84 pages

Compressed Sampling is an emerging method of reconstructing data that have large size and/or contain missing, noisy or irregular values using a small set of data. This method uses sparsity of data and realizes reconstruction process very efficiently. After a few samplings of data, it uses an optimization algorithm for reconstruction. This method has been used in areas like signal processing, image/video processing and medical imaging intensively.

Bidirectional Reflectance Distribution Function (BRDF) data is used to describe different reflectance properties of real world materials. In this work, the reconstruction process of large sized and sparse structured BRDF data is realized using compressed sampling method. This method also reconstructs missing, irregular or noisy values in BRDF data effectively. Furthermore in this work, using two of existing BRDF models, BRDF data are created and reconstructed successfully using compressed sampling method.

Keywords: Compressed Sampling, Compressive Sensing, Bidirectional Reflectance Distribution Function, BRDF data, data reconstruction

ÖZET

KAYIP BRDF ÖLÇÜMLERİNİN SIKIŞTIRMALI ÖRNEKLEME YÖNTEMİYLE TAHMİN EDİLMESİ

Nurcan SEYLAN

Doktora Tezi, Bilgisayar Mühendisliği Bölümü

Tez Danışmanı: Prof. Dr. Mehmet Cudi OKUR

Eylül 2015, 84 sayfa

Sıkıştırımlı Örnekleme, büyük miktarlardaki ve/veya kayıp, gürültülü veya geçersiz değerler içeren verinin küçük bir kısmını kullanarak bu veriyi yeniden oluşturmayı sağlayan yeni bir metottur. Bu metot, verinin seyrek (sparse) olmasını kullanır ve çok etkin bir yeniden oluşturma işlemi gerçekleştirir. Verinin az sayıdaki örneklemelelerinden sonra bir eniyileme algoritması kullanılarak veri yeniden elde edilir. Bu yöntem şimdiye kadar sinyal işleme, resim/video işleme, tıbbi görüntüleme gibi alanlarda yoğun olarak kullanılmıştır.

Çift Yönlü Yansıma Dağılım Fonksiyonu (BRDF) verisi, gerçek materyallerin farklı yansıma özelliklerini tanımlamak için kullanılır. Bu çalışmada, sıkıştırımlı örnekleme yöntemi kullanılarak, büyük boyutlu ve seyrek yapıdaki BRDF verisinin yeniden oluşturulması işlemi gerçekleştirilmiştir. Ayrıca bu yöntemle bu verinin içerdiği kayıp, geçersiz, gürültülü değerler etkili bir şekilde yeniden oluşturulabilmektedir. Bunun dışında mevcut BRDF modellerinden ikisi kullanılarak BRDF verisi oluşturulmuş ve sıkıştırımlı örnekleme yöntemiyle başarılı bir şekilde yeniden oluşturulmuştur.

Anahtar sözcükler: Sıkıştırımlı Örnekleme, Çift Yönlü Yansıma Dağılım Fonksiyonu, BRDF verisi, veriyi yeniden oluşturma

ACKNOWLEDGEMENTS

First of all, I would like to thank first supervisor of my doctorate studentship and my thesis, Prof. Aydın Öztürk, for his invaluable support, help and encouragement throughout the years.

I would like to express my gratitude to my latter supervisor, Prof. Mehmet Cudi Okur, for his great support and help on my thesis.

I would also like to thank committee member of my thesis, Assist. Prof. Korhan Karabulut, for his support and time.

In addition, I would like to thank the Department of Computer Engineering at Yaşar University.

I thankfully acknowledge the great support and time of research assistant Serkan Ergun, PhD at International Computer Institute, Ege University during my thesis period.

This thesis would not have been possible without these people's encouragement and support.

Finally, of course my deepest gratitude is for my family, thanks for their patience and encouragement throughout the years.

Nurcan SEYLAN
İzmir, 2015

TEXT OF OATH

I declare and honestly confirm that my study, titled “Estimating Missing BRDF Measurements with Compressed Sampling Method” and presented as a Doctorate Thesis, has been written without applying to any assistance inconsistent with scientific ethics and traditions, that all sources from which I have benefited are listed in the bibliography, and that I have benefited from these sources by means of making references.

TABLE OF CONTENTS

	Page
ABSTRACT	iii
ÖZET	iv
ACKNOWLEDGEMENTS	v
TEXT OF OATH	vi
TABLE OF CONTENTS	vii
INDEX OF FIGURES	x
INDEX OF TABLES	xiii
INDEX OF SYMBOLS AND ABBREVIATIONS	xiv
1 INTRODUCTION	1
2 COMPRESSED SAMPLING	5
2.1 Data Acquisition Using Conventional Method	5
2.2 Data Acquisition Using Compressed Sampling Method	6
2.2.1 Compressible Signals	7
2.2.2 Designing A Measurement Matrix	7
2.2.3 Restricted Isometry Condition (RIC)	9
2.2.4 The Geometry of l_1 Optimization	11

2.3	Recent Developments of CS	12
2.4	Applications of CS	12
3	BRDF (Bidirectional Reflectance Distribution Function)	20
3.1	Properties of BRDFs	21
3.2	Analytic reflectance models	21
3.3	Fitting BRDF Data to Analytical Models	22
3.4	BRDF Measurement	23
3.5	Problems Associated with BRDF Measurements	26
3.6	Reflectance Representations	27
3.7	An Alternative Data Representation	27
4	COMPRESSED SAMPLING AND BRDF DATA	31
4.1	Reconstruction of Brdf Values	31
4.2	Reconstruction of Sampled Real BRDF Data	33
5	CS AND BRDF DATA OF ANALYTIC REFLECTANCE MODELS	39
5.1	Ward Model	39
5.2	Reconstruction of BRDF Data Obtained by Ward Model	40
5.3	Cook-Torrance Model	41
5.4	Reconstruction of BRDF Data Obtained by Cook-Torrance Model	41

6	CONCLUSION	43	
	REFERENCES	44	
	APPENDICES	48	
	APPENDIX – 1	Original and reconstructed images and associated PSNR values for selected six materials	49
	APPENDIX – 2	Original and reconstructed images and associated PSNR values Using LogTransformation for selected six materials	52
	APPENDIX – 3	Reconstructed images and difference images (in insets) and associated PSNR values for selected 24 materials and for 5% sampling ratio	55
	APPENDIX – 4	Original and reconstructed images acquired using 5% and 2.5% reconstruction ratios and associated PSNR values for 34 materials	57
	APPENDIX – 5	Results of Reconstruction of BRDF Data Obtained by Ward Model	66
	APPENDIX – 6	Results of Reconstruction of BRDF Data Obtained by Cook-Torrance Model	76
	CURRICULUM VITEA	84	

INDEX OF FIGURES

Figure 2.1 Coefficients of the wavelet of an image (Mackenzie, 2009). 6

Figure 2.2 (a) CS measurement process with a random Gaussian matrix Φ and a DCT matrix Ψ . The vector s is sparse with $k = 4$. (b) Reconstruction process with $\Theta = \Phi\Psi$. There are four columns of matrix Θ and they correspond to nonzero s_i coefficients; the vector y is a combination of these columns (Baraniuk, 2007). 8

Figure 2.3 (a) A very sparse vector. If this vector is sampled directly with no knowledge, values that are very close to zero are obtained. (b) Examples of random, incoherent test vectors ϕ_k . With each inner product of a vector from (b) a little bit of information about (a) is get each time (Romberg, 2008). 10

Figure 2.4 (a) l_1 ball of radius r ; the ball contains all α such that $|\alpha(1)| + |\alpha(2)| \leq r$. (b) Solving the l_1 minimization problem allows to reconstruct a sparse α_0 from $y = \Phi\alpha_0$, as the anisotropy of the l_1 ball favors sparse vectors. (c) Minimizing the l_2 norm does not recover α_0 , since the l_2 ball is isotropic, the l_2 minimization $\alpha^*_{l_2}$ will in general not be sparse at all (Romberg, 2008). 11

Figure 2.5 The structure of the single-pixel camera. The “DMD” is the grid of micro-mirrors that reflect some parts of the incoming light beam toward the sensor randomly. Other parts of the image that are not reflected (the black squares) are diverted away. Each measurement made by the photodiode is a random combination of a great number of pixels (Mackenzie, 2009). 13

Figure 2.6 (a) Frame 32 of a 64-frame video sequence (64x64 images of a disk moving, thereby 262,144 3-D voxels). (b) CS frame-by-frame reconstruction by obtaining 20,000 total 2-D random projections. (c) Full 3-D video reconstruction by obtaining 20,000 3-D random projections (using CS and 3-D wavelets). (d) Result of using 3-D wavelets (Wakin et al. 2006). 14

Figure 2.7 Images belonging to an angiogram. From bottom to top, the angiogram is increasingly undersampled by larger ratios. With a Shannon-Nyquist sampling strategy, the image degrades as the ratio of undersampling increases. With compressed sensing, the image remains very sharp even at 20-fold undersampling (Mackenzie, 2009). 15

Figure 2.8 (a) The raw echo signal with sampling rate 12 MHz (b) The reconstructed signal with sampling rate 4 MHz (Lv and Wu, 2012). 16

Figure 2.9 Activated brain areas for various methods and acceleration ratio. (SW: Sliding Window, ME/MC: Motion Estimation/Compensation) (Jung and Ye, 2009). 18

Figure 2.10 Hashing schema (Kang et al. 2009). 19

Figure 3.1 Four angles to describe a BRDF (Matusik et al. 2003). 20

Figure 3.2 BRDF Measurement system of Matusik et al. The system is placed in a completely isolated room painted in black matte (Matusik et al., 2003). 24

Figure 3.3 Pictures of the 100 acquired materials from Matusik BRDF Database (Matusik et al., 2003). 24

Figure 3.4 CURET dataset (2007). 61 materials are used in BRDF measurements. 25

Figure 3.5 BRDF Measurement system of Marschner et al (Marschner et al. 2000). 26

Figure 3.6 The standard coordinate system is shown on the left. Rusinkiewicz's coordinate system is shown on the right (Matusik et al. 2003). 28

Figure 3.7 Rendered teapots using BRDFs from Matusik's database: Nickel, hematite, gold paint and pink fabric (Matusik et al. 2003). 29

Figure 3.8 A visual and PSNR comparisons of some well-known BRDF representations on the Princeton scene (Kurt, 2014). 29

Figure 3.9 Based on BRDF modeling, photo-realistic renderings are generated for metallic car paint (Rump et al. 2008).	30
Figure 4.1 Left: Presentation of calculated BRDF values, Right: After CS reconstruction using 30% of BRDF values, acquired BRDF values.	31
Figure 4.2 Results of various sampling ratios for chrome-steel material. Images have lighting artifacts even at 10% sampling ratio.	34
Figure 4.3 Results of various sampling ratios for chrome-steel material after using Log Transformation. Images don't have lighting artifacts beginning from 5% sampling ratio.	35
Figure 4.4 Above 0.05 ratio for all materials have sufficient PSNR values.	36
Figure 4.5 A sample scene has been rendered using alum-bronze and blue-metallic-paint materials. Top: Image based on the original data. Bottom: Image based on the reconstructed data using only 5% of the original data (PSNR is 51.63 dB).	38

INDEX OF TABLES

Table 4.1 PSNR Results of Reconstruction of BRDF Data of Selected Six Materials	34
Table 4.2 PSNR Results of Reconstruction of BRDF Data of The Same Six Materials Using Log Transformation	35
Table 4.3 PSNR Results of Reconstruction of Using 5% of BRDF Data of 24 Sample Materials	36
Table 4.4 PSNR Results of Reconstruction of Using 2.5% and 5% of BRDF Data of 34 Sample Materials	37
Table 5.1 PSNR Results of Reconstruction of BRDF Data Obtained by Ward Analytic Model	40
Table 5.2 PSNR Results of Reconstruction of BRDF Data Obtained by Cook-Torrance Analytic Model	42

INDEX OF SYMBOLS AND ABBREVIATIONS

<u>Symbols</u>	<u>Explanations</u>
Ψ	Basis matrix used in CS
Φ	Sampling matrix used in CS
Θ	Measurement matrix used in CS
l_0 -norm	The number of non-zero entries in a vector
l_1 -norm	Absolute-value norm
l_2 -norm	Euclidean norm
θ_i	Incoming light angle for BRDF
θ_o	Outgoing light angle for BRDF
Φ_{diff}	Azimuth difference angle for BRDF

Abbreviations

BRDF	Bidirectional Reflectance Distribution Function
CS	Compressed Sampling / Compressive Sensing
DCT	Discrete Cosine Transform
DMD	Digital Micromirror Device

fMRI	Functional Magnetic Resonance Imaging
MSE	Mean Squared Error
norm	l_2 -norm
OMP	Orthogonal Matching Pursuit
Org	Original
PSNR	Peak-Signal-to-Noise-Ratio
Rec	Reconstructed
RIC	Restricted Isometry Condition
ROMP	Regularized OMP
VIF	Visual Information Fidelity
2-D	2-Dimensional
3-D	3-Dimensional

1 INTRODUCTION

Real world materials have different reflection properties. Bidirectional Reflectance Distribution Function (BRDF) that is defined in terms of incoming and outgoing light directions is commonly used to describe reflectance properties of real world materials. Physically based analytic reflectance models or empirical analytic reflectance models have been proposed for approximating the BRDF.

An alternative approach for modeling surface reflection is to directly measure values of the BRDF for different incoming and outgoing angles and then fit the selected analytic model to the measured data by using appropriate optimization techniques. There are some drawbacks to this measure-and-fit approach. The choice of the error function which the optimization process uses is very important. Also, since most BRDF models are non-linear, the optimization phase used in the fitting process relies excessively on the initial guess for the model parameters. In some cases measurements for which incident or outgoing angles greater than 80 degrees are ignored. Measurements corresponding to these grazing angles are in general unreliable since they contain much more noisy, missing or irregular values. Also sufficient amount of BRDF data are difficult to obtain and low sampling rates make the BRDF fitting inadequate and the result is excessively dependent on the choice of the model.

The third approach for modeling surface reflectance is to obtain dense measurements of reflectance and use these measurements directly as a BRDF. This method preserves the elaborateness of the reflectance function that is lost in a data-fitting approach. The classical device for measuring BRDF is the gonio-reflectometer, which consists of a photometer and light source that are moved around a surface sample under computer control. Such devices measure only a radiance value at a time and this work makes this process very time-consuming. Also an important difficulty about the BRDF data is its large size. The method of using BRDF measurements becomes more expensive if the reflectance for all materials in a scene needs to be measured. On the other hand, the BRDF data obtained in this way is generally noisy and contains some missing values due to some difficulties in measuring BRDF especially near grazing angles (Rusinkiewicz, 1997). BRDF measuring systems also

suffer from occlusion problems because of using cameras, projectors and mirrors. In such cases, obtaining all BRDFs over a full hemisphere may not be possible and measurements taken at certain angles may be very noisy and cannot be used for rendering. The main advantage of this method is that it produces realistic images, since acquired BRDFs come from real measured data (Matusik, 2003).

Even if the raw data are correct and complete, its size is considerably large to store and process. An alternative approach is to compress the measured BRDF data using some compression techniques. These techniques are based on using basis functions (like splines, wavelets, spherical harmonics and Zernike polynomials), dimension reduction techniques (like Principal Component Analysis, Independent Component Analysis and Cluster Analysis) and matrix factorization (like Non-negative Matrix Factorization and Tensor Products) (Seylan et al. 2013). However none of these techniques can represent noisy, missing or irregular measurements completely. Therefore measurements that have problems need to be preprocessed.

In this work, a new technique called Compressed Sampling is proposed to use for reconstructing noisy BRDF data with some missing measurements. This technique also provides an efficient way of compressing the BRDF data. It is proven that even with noisy measurements and compressible (but not very sparse) signals, compressed sensing works quite well (Candès et al. 2006). It has been applied to problems in areas like compressive imaging, video processing, medical imaging, computer vision and wireless channel mapping.

The theory of Compressed Sampling states that if a signal is sparse in a transform domain, then under certain conditions it can be reconstructed exactly from a small set of linear measurements using some tractable optimization algorithms. These measurements are random samplings of BRDF data. An l_1 -norm optimization algorithm is used for optimization.

In this work, the compressed sampling technique is applied on isotropic BRDF data which is assumed to have some missing measurements. For this purpose, three dimensional data of various materials are divided into sub-sample blocks. Two of dimensions are for incoming and outgoing direction angles with surface normal and one dimension is for azimuth difference angle. Random samples are generated from

these sub-samples at a predefined sampling ratio with point sampling based on using a permutation matrix. A permutation matrix is an $m \times n$ binary matrix that has maximum one entry of 1 (one) in each row and each column and 0s elsewhere, ones corresponding to the measurements to be considered. This matrix is used to represent a specific permutation of m elements and, when used to multiply a vector, can produce that permutation in a column vector. The permutation matrix is modified to discard the missing or noisy measurements from the generated samples. Finally, the resulting random samples are used to reconstruct the BRDF data running the compressed sampling technique.

To investigate the effect of the sampling ratio on the visual quality of the reconstructed images, random samples with different ratios are generated for randomly selected 40 different isotropic materials. These materials are chosen to reflect the diffuse, glossy and specular properties of reflection. PSNR (Peak-Signal-to-Noise-Ratio) values between original and reconstructed images are used for visual quality comparison. 5% ratio is readily sufficient for diffuse and glossy materials on the average; but for specular materials, even 10% ratio is not sufficient. The reason of this situation is some data sets has more irregular values as a result of certain measurement errors and these irregular values cause lighting artifacts. To correct this situation, log transformation of the BRDF measurements is used. After reconstruction the log transformation is reversed.

Using log transformation, it is interesting to see that images with a visually acceptable quality and PSNR values could be obtained by sampling only 2.5% of the measurements for diffuse and glossy materials. Especially for diffuse materials even 1% sampling ratio has successful results and for specular materials 5% sampling ratio is sufficient generally.

These results demonstrate the power of the compressed sampling approach when dealing with BRDF data having missing measurements. Compressed sampling approach produces visually acceptable quality and sufficient PSNR values for all material types by sampling only 5% of the original data.

In the field of computer graphics, surface reflectance has been approximated frequently with analytic reflectance models. These BRDF models produce

approximations of reflectance of real materials. In this work, Ward and Cook-Torrance BRDF models that are extensively used are selected and BRDF data for various materials are constructed using these models respectively.

For 40 materials that are selected previously, using their Ward and Cook-Torrance parameters respectively, BRDF values are calculated separately and then using low sampling ratios of each data, BRDF data are reconstructed for each material. Using Ward model data, 2.5% sampling ratio produces visually acceptable quality and high PSNR values for approximately all materials. Using Cook-Torrance model data, 5% sampling ratio produces visually acceptable quality and high PSNR values for most materials and similar results are obtained with 10% sampling ratio for the others.

Last of all, in this study, very successful results have been obtained using Compressed Sampling technique with low sampling ratio of measured BRDF data and also BRDF data generated from reflectance models.

The rest of the thesis is organized as follows: In Chapter 2, the theory of Compressed Sampling is described in detail and recent developments and some applications of this technique are outlined.

In the third chapter, the BRDF properties, analytic reflectance models, BRDF measurements and problems about these measurements are explained.

In chapter 4, Compressed Sampling application on BRDF data and the corresponding results are explained.

In chapter 5, results based on applying Compressed Sampling technique on the BRDF data generated from two different analytic reflectance models are presented.

Chapter 6 is devoted for discussion of results and conclusion.

2 COMPRESSED SAMPLING

2.1 Data Acquisition Using Conventional Method

The origin of Compressed Sampling begins in 1949, with Claude E. Shannon, the developer of information theory. Shannon proved that a signal with N hertz maximum frequency can be excellently reconstructed by sampling the signal at intervals of $1/2N$ seconds (Mackenzie, 2009). In other words, it is specified that to beware losing information when capturing a signal, it must be sampled at least two times more than the signal bandwidth. Using this rate, results too many samples, making compression an obligation prior to storage and transmission (Baraniuk, 2007).

As a result, within data acquisition process, generally large amounts of data are collected to be discarded at the compression stage. A high-resolution data array is acquired, the complete set of transform coefficients are computed, the largest coefficients are encoded and all the others are discarded. This process of large amount of data acquisition followed by compression is considerably wasteful (Candès & Wakin, 2008).

If no information about the signal or image trying to reconstruct is available, then Shannon's theorem limits the resolution that must be acquired. But if the signal or image is sparse or compressible, then Shannon's limit is not an obligation.

For instance, photographs are not sparse relative to the standard basis; because they have many nonzero values (i.e., non-black pixels). However, according to JPEG compression, photographs are sparse with respect to a different basis.

One of the compression procedure examples is to represent the image as a sum of wavelets. The coefficients of wavelet of an image is plotted in figure 2.1, large coefficients identifies a considerable contribution to the image (such as an edge or a texture). Mostly it is impossible to distinguish the difference between the compressed photo and the original photo (Mackenzie, 2009).

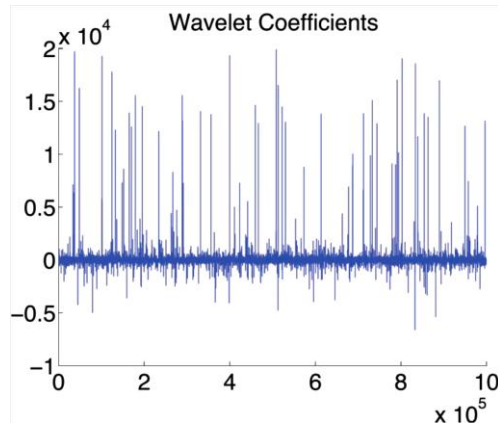


Figure 2.1 Coefficients of the wavelet of an image (Mackenzie, 2009).

2.2 Data Acquisition Using Compressed Sampling Method

In the Compressed Sampling side, the obtainable resolution is controlled by the information content of the signal. A signal with low information content can be reconstructed excellently by using a small number of measurements. For instance, almost all real-world images have low information content. It is possible to contain the content of the image with a small number of identifiers.

First of all, Emmanuel Candès, a former student of Donoho, in 2004, while working with a team of radiologists on magnetic resonance imaging; and running with a “phantom image” (i.e., not a real patient), he had reconstructed the image perfectly from undersampled data using Compressed Sampling (Mackenzie, 2009).

The theory of Compressed Sampling / Sensing (CS) demonstrates how a subsampled signal can be accurately reconstructed through non-linear optimization techniques (Sen & Darabi, 2009). For this, CS technique uses the sparsity property of the signals. A signal is represented as a vector \mathbf{x} , a series of n real numbers. This vector is said to be *k-sparse*, which means that it has at most k nonzero coefficients in a specific basis (Mackenzie, 2009).

For example, transform coders such as JPEG2000 take advantage of the fact that many signals are sparse in a fixed basis, meaning that it can be stored or transmitted only a small number of transform coefficients rather than all the signal samples (Candès, 2006).

2.2.1 Compressible Signals

A one-dimensional, discrete signal \mathbf{x} can be viewed as an $n \times 1$ column vector with elements $x[i]$, $i = 1, 2, \dots, n$. An image or higher-dimensional data is vectorized into a long one-dimensional vector.

The signal \mathbf{x} is *k-sparse* if it is a linear combination of only k basis vectors; so, only k of the s_i coefficients in Eq. 2.1 are nonzero and $(n - k)$ are zero. It is meaningful for CS if k is much less than n .

For this, the vector \mathbf{x} can be transformed into another $n \times 1$ vector \mathbf{s} through an $n \times n$ orthogonal basis matrix Ψ as

$$\mathbf{x} = \Psi \mathbf{s} \quad (2.1)$$

\mathbf{s} is the $n \times 1$ column vector of weighting coefficients. Since Ψ is orthogonal, the equation 2.1 can be solved for \mathbf{s} as $\mathbf{s} = \Psi' \mathbf{x}$ where Ψ' is the transpose of Ψ . If \mathbf{s} can be estimated from the sample data then \mathbf{x} can be reconstructed from the above equation (Seylan et al. 2013). The underlying approach provides a non-adaptive technique where the entries of the matrix Ψ are fixed.

Compressed Sampling directly acquires a compressed signal representation without going through the phase of acquiring n samples (Baraniuk, 2007).

2.2.2 Designing A Measurement Matrix

A sample \mathbf{y} of the signal \mathbf{x} , is a linear function of \mathbf{x} , that is,

$$\mathbf{y} = \Phi \mathbf{x} \quad (2.2)$$

The number of measurements in the sample is arranged to be smaller than the signal, therefore Φ is an $m \times n$ matrix with $m \ll n$ and \mathbf{y} is an $m \times 1$ vector. According to linear algebra, there are infinitely different vectors \mathbf{x} such that $\Phi \mathbf{x} = \mathbf{y}$ (Mackenzie, 2009).

However, a key hypothesis of compressed sensing is that the transformed version of the signal, \mathbf{s} , is k -sparse under some basis Ψ , meaning that it has at most k nonzero coefficients in that basis.

The measurement process using Eq. 2.1 is as:

$$\mathbf{y} = \Phi \mathbf{x} = \Phi \Psi \mathbf{s} = \Theta \mathbf{s} \quad (2.3)$$

where $\Theta = \Phi \Psi$ is a general $m \times n$ measurement matrix (Sen & Darabi, 2009).

The signal reconstruction algorithm must take the m measurements in the vector \mathbf{y} , the sampling matrix Φ , and the basis matrix Ψ and reconstruct the $length$ - n sparse coefficient vector \mathbf{s} . An example is shown in figure 2.2.

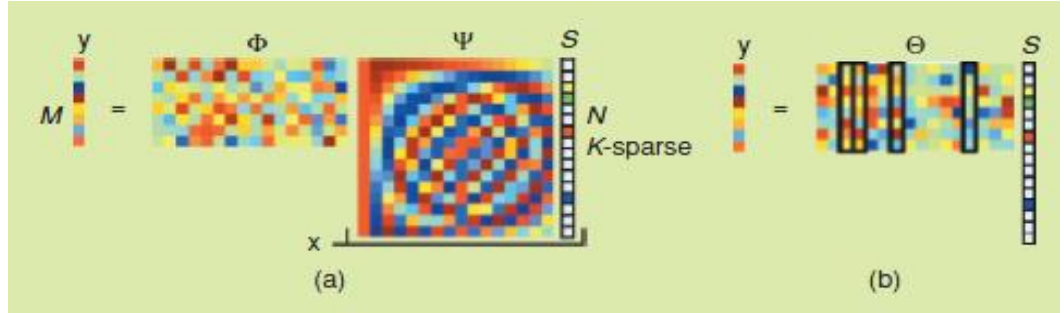


Figure 2.2 (a) CS measurement process with a random Gaussian matrix Φ and a DCT matrix Ψ . The vector \mathbf{s} is sparse with $k = 4$. (b) Reconstruction process with $\Theta = \Phi \Psi$. There are four columns of matrix Θ and they correspond to nonzero s_i coefficients; the vector \mathbf{y} is a combination of these columns (Baraniuk, 2007).

If \mathbf{s} can be solved by giving the measured \mathbf{y} , the inverse transform $\Psi \mathbf{s}$ can be applied to get desired signal \mathbf{x} . Unfortunately, traditional techniques for solving for \mathbf{s} (e.g., inversion, least squares) do not work because Eq. 2.3 is severely undetermined since $m \ll n$. However, recent improvements in CS have shown that if $m \geq 2k$ and Θ has certain properties (e.g. RIC property, that is explained in Section 2.2.3: Restricted Isometry Condition), then Eq. 2.3 can be solved uniquely for \mathbf{s} by looking for the sparsest \mathbf{s} . Therefore, the desired \mathbf{s} can be found by solving the following l_0 -optimization problem (l_0 -norm counts the number of non-zero entries):

$$\min \|\mathbf{s}\|_0 \quad \text{s.t.} \quad \mathbf{y} = \Theta \mathbf{s} \quad (2.4)$$

The solution to this problem is a combinatorial algorithm in which every \mathbf{s} with $\|\mathbf{s}\|_0 \leq k$ is checked to find the one that results the measured samples \mathbf{y} . This problem is *NP-complete* and is intractable for any applicable signal. Eq. 2.3 can be solved by replacing the l_0 with an l_1 -norm (l_1 -norm of \mathbf{x} : $\sum |\mathbf{x}_i|$):

$$\mathbf{min} \|\mathbf{s}\|_1 \quad \text{s.t.} \quad \mathbf{y} = \Theta \mathbf{s} \quad (2.5)$$

l_1 -norm is used in (2.5) because sparse signals have small l_1 -norms and it is convex which makes the optimization problem computationally tractable. As long as the number of samples $m = O(k \log n)$ and the matrix Θ meets the RIC property, the l_1 -optimization of Eq. 2.5 will solve correctly for \mathbf{s} (Sen & Darabi, 2009).

l_1 -norm optimization tends to concentrate the energy of the signals onto a few nonzero entries of \mathbf{s} as opposed to the least squares which tends to spread the energy around.

Unfortunately, l_2 -minimization (l_2 -norm is Euclidean norm: $|\mathbf{x}|$) cannot find a *k-sparse* solution, returning instead a non-sparse \mathbf{s} with many nonzero elements. (See Section 2.2.4: The Geometry of l_1 Optimization)

2.2.3 Restricted Isometry Condition (RIC)

$\mathbf{y} = \Theta \mathbf{s}$ cannot be solved for \mathbf{s} with any arbitrary Θ if $m \ll n$, even if $m \geq 2k$. However, within the compressed sensing framework if matrix Θ meets the Restricted Isometry Condition (RIC):

$$(\mathbf{1} - \epsilon)\|\mathbf{v}\|_2 \leq \|\Theta \mathbf{v}\|_2 \leq (\mathbf{1} + \epsilon)\|\mathbf{v}\|_2 \quad (2.6)$$

where $\epsilon \in (0, 1)$ for all z -sparse vectors \mathbf{v} . A measurement matrix is valid for CS if every possible set of z columns of Θ forms an approximate orthogonal set. For this, the sampling matrix Φ must be as incoherent to the compression basis Ψ as possible. The coherency measures the largest correlation between any two elements. If Φ and Ψ contain correlated elements, it means that the coherency is large. Random matrices are substantially incoherent with any basis matrix Ψ . Examples of matrices that have been proven to meet incoherency include Gaussian matrices (sampled from a normal

distribution), Bernoulli matrices (sampled from a Bernoulli distribution), and partial Fourier matrices (randomly selected Fourier basis functions) (Sen & Darabi, 2009). Gaussian matrix provides that k -sparse signals of length n can be reconstructed using only $m \times 1$ vector \mathbf{y} where $m \geq ck \log(n/k) < n$ and c is a small constant random number.

In figure 2.3: if it cannot be known where the important values are, sampling the transform coefficients in (a) directly will be a useless effort, because most of the time values that are very close to zero are seen. If instead global combinations of the transform coefficients are taken, an effect achieved by using incoherent ϕ_k as illustrated in (b), a little bit of information about the sparse coefficient sequence is picked up with each measurement. The Eq. 2.3 then finds the locations of important transform coefficients and their values (Romberg, 2008).

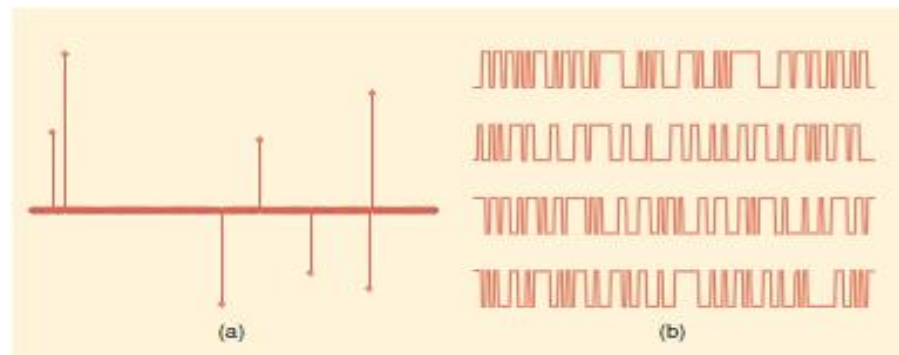


Figure 2.3 (a) A very sparse vector. If this vector is sampled directly with no knowledge, values that are very close to zero are obtained. (b) Examples of random, incoherent test vectors ϕ_k . With each inner product of a vector from (b) a little bit of information about (a) is get each time (Romberg, 2008).

The randomness of the sampling matrix Φ is also useful for two purposes. First, it provides the set of conditions under which l_1 -minimization is equivalent to l_0 -minimization. Secondly, it provides that the set of measurement vectors (the rows of Φ) are as dissimilar to the basis vectors (the columns of Ψ) as possible (Mackenzie, 2009).

2.2.4 The Geometry of l_1 Optimization

In figure 2.4, the geometric illustration for l_1 is seen. (a) illustrates the l_1 ball of a certain radius. It is anisotropic; it is pointy along the axes. (b) diagrams the l_1 recovery program: the point labeled α_0 is a “sparse” vector (only one of its components are nonzero) of which one measurement is made; the line labeled H is the set of all α that share the same measurement value.

For equation 2.5, the point on this line with minimum l_1 norm is picked out. To visualize how equation 2.5 accomplishes this, an l_1 ball of tiny radius is taken and is expanded gradually until it bumps into H. This first point of intersection is the vector that solves equation 2.5. Both of the anisotropy of the l_1 ball and the flat space H result this intersection occurring at one of the points, exactly where sparse signals are located.

If the l_1 norm is replaced with the l_2 norm, figure 2.4 (c) replaces the diamond-shaped l_1 ball with the spherical and perfectly isotropic l_2 ball. It is seen that the point of first intersection of H and the expanding l_2 ball is not sparse (Romberg, 2008).

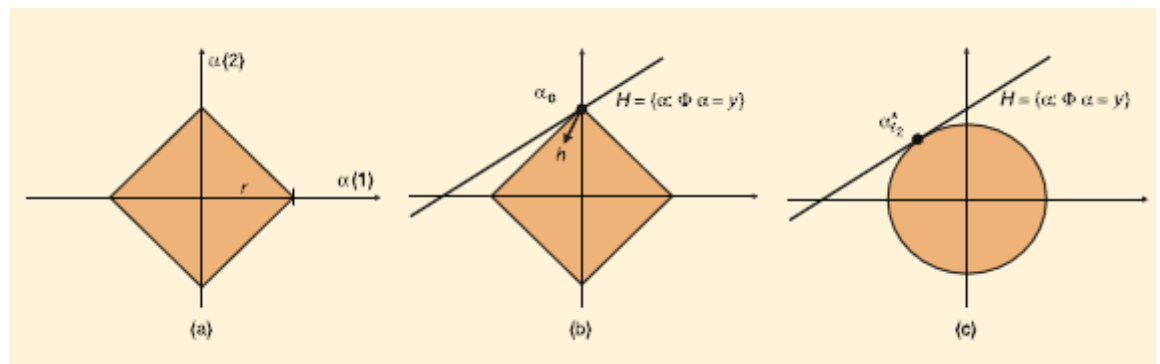


Figure 2.4 (a) l_1 ball of radius r ; the ball contains all α such that $|\alpha(1)| + |\alpha(2)| \leq r$. (b) Solving the l_1 minimization problem allows to reconstruct a sparse α_0 from $y = \Phi \alpha_0$, as the anisotropy of the l_1 ball favors sparse vectors. (c) Minimizing the l_2 norm does not recover α_0 , since the l_2 ball is isotropic, the l_2 minimization $\alpha_{l_2}^*$ will in general not be sparse at all (Romberg, 2008).

2.3 Recent Developments of CS

Donoho, Candès, Tao and Romberg studied on CS firstly announcing similar results during 2004-2006 (Candès, 2006; Donoho, 2004; Candès et al. 2006). Since then, there have been many advances in terms of theory and practice.

Candès, Romberg, and Tao proved that even with noisy measurements and compressible (but not very sparse) signals, compressed sensing works quite well. The error in the reconstructed signal is not much bigger than the error in the measurements, and the error with using the l_1 -minimizer is not much bigger than the error already revealed by the l_0 -minimizer. In other words, the l_1 -minimizer accurately recovers the largest components of the signal.

Mathematicians have been working on new algorithms that run faster than the standard linear programming methods that solve the l_1 -minimization problem. Instead of getting the largest k coefficients all at once, these coefficients are found iteratively: first the largest nonzero coefficient, then the second largest nonzero coefficient, and so on (Mackenzie, 2009). The first such algorithm, called Orthogonal Matching Pursuit (OMP), has a weaker guarantee of exact recovery compared to l_1 -minimization (Tropp & Gilbert, 2007). However, there is now a variety of OMP, such as Regularized OMP (ROMP) which recovers multiple coefficients in each iteration; thus accelerates the algorithm and successfully combines the accuracy of l_1 -minimization with the speed of OMP (Needell & Vershynin, 2007).

2.4 Applications of CS

Since Compressed Sensing had begun a few years ago, it has been applied to problems in compressive imaging, video processing, medical imaging and wireless channel mapping. It is also used in the computer vision and graphics applications to solve problems in face recognition and light transport acquisition (Sen & Darabi, 2009).

Academicians in different fields are developing practical applications of compressed sensing. Baraniuk and Kelly's single-pixel camera which is built in 2006, uses an array of micro-mirrors to acquire a random sample of the incoming light

(Figure 2.5) (Baraniuk, 2007). Each mirror can be tilted in one of two directions, either to reflect the light toward the sensor or far away from it. Thus the light that the sensor receives is a weighted average of many distinct pixels, all combined into as one pixel. By taking $k \cdot \log(n/k)$ measurements as snapshots, with a different random selection of pixels each time, the single-pixel camera is able to acquire a considerably recognizable picture (Mackenzie, 2009).

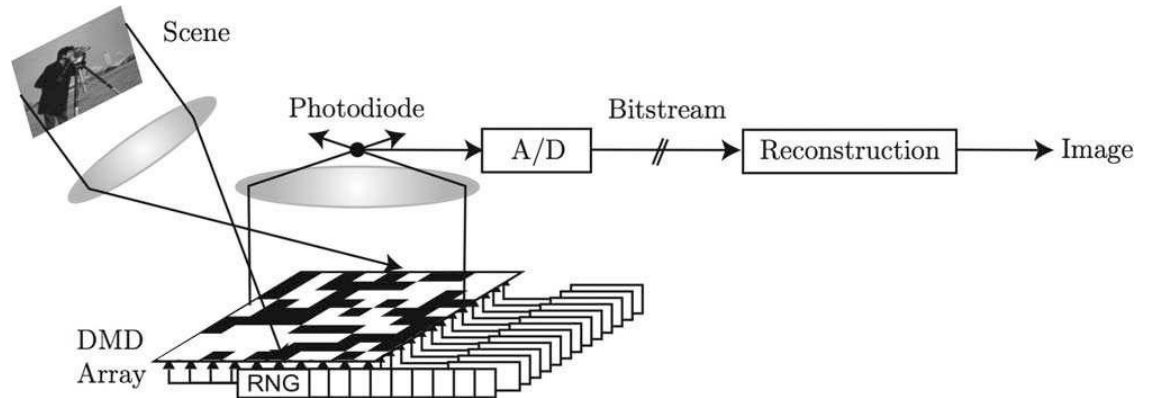


Figure 2.5 The structure of the single-pixel camera. The “DMD” is the grid of micro-mirrors that reflect some parts of the incoming light beam toward the sensor randomly. Other parts of the image that are not reflected (the black squares) are diverted away. Each measurement made by the photodiode is a random combination of a great number of pixels (Mackenzie, 2009).

Sen and Darabi’s framework measures a subset of the pixels in the photograph and uses compressed sensing algorithms to reconstruct the entire image from this data. In this work, ROMP technique is used. Initially, the Fourier basis is used because the Fourier basis is incoherent with the point-sampling basis Φ (wavelets are not). This works well for artificially-sparsified images and is able to produce almost perfect reconstructions. However, when working with real images that are not sparsified, the algorithm fails, performing worse than bilinear interpolation. To overcome this problem an algorithm that performs considerably better than bilinear interpolation is developed. For this, a wavelet basis is used for compression, which offers increased sparsity. But, wavelets are not incoherent with point-samples. To reduce the coherence between Φ and Ψ , measurement process is changed to include an invertible filtering process before sampling (Sen & Darabi, 2009).

Ivan Lee’s work investigates the performance of weighted compressive video sensing, which brings the function of predicted frames and bi-directional predicted

frames in traditional video codecs to compressive video sensing. A masking disk simplifies coding of region-of-interest which can be managed both at the encoder and the decoder. Due to similarities between adjacent video frames, measurements can be reused to develop the reconstructed video quality. Instead of applying interpolation techniques, measurement in CS-domain is used at the decoder (Lee, 2011).

In another work, a new digital image/video camera that directly acquires random projections of signals without first acquiring the whole pixels/voxels is used. The camera employs a digital micromirror array to perform linear projections of an image onto random binary patterns. This significantly reduces the computation time and cost that is required intensively for video acquisition/encoding.

The camera takes streaming measurements of a video signal that can be recovered using CS techniques designed for either 2-D frame-by-frame reconstruction or joint 3-D reconstruction.

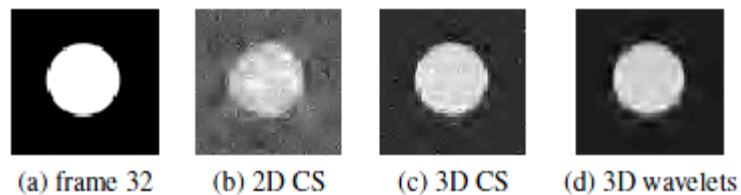


Figure 2.6 (a) Frame 32 of a 64-frame video sequence (64x64 images of a disk moving, thereby 262,144 3-D voxels). (b) CS frame-by-frame reconstruction by obtaining 20,000 total 2-D random projections. (c) Full 3-D video reconstruction by obtaining 20,000 3-D random projections (using CS and 3-D wavelets). (d) Result of using 3-D wavelets (Wakin et al. 2006).

It is seen in Figure 2.6 that 3-D reconstruction significantly outperforms 2-D frame-by-frame reconstruction, since a 3-D video wavelet transform is sparser than a union of 2-D image wavelet transforms (Wakin et al. 2006).

Compressed sensing has been used by medical imaging applications; also the theory is directly inspired by a problem in magnetic resonance imaging. MRI

scanners have conventionally been limited to imaging static structures over a short period of time, and the patient has been told to hold his or her breath. But, by treating the image as a sparse signal in space and time now, MRI scanners have overcome these limitations and produce images like a beating heart. Figure 2.7 shows how a CS reconstruction algorithm can provide a sharp image of the arteries in a patient's leg even with 20 times less data than a conventional angiogram (Mackenzie, 2009).

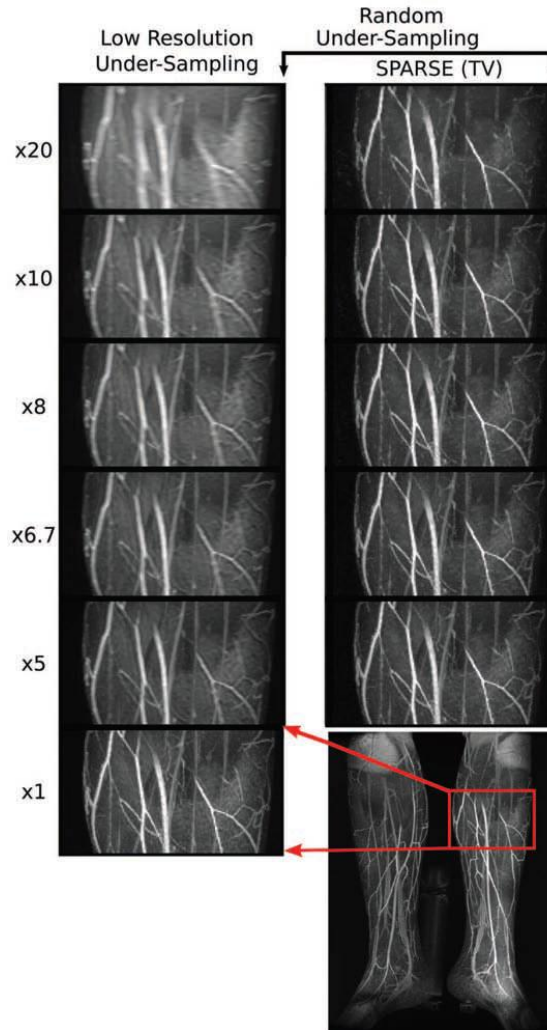


Figure 2.7 Images belonging to an angiogram. From bottom to top, the angiogram is increasingly undersampled by larger ratios. With a Shannon-Nyquist sampling strategy, the image degrades as the ratio of undersampling increases. With compressed sensing, the image remains very sharp even at 20-fold undersampling (Mackenzie, 2009).

Kirolos et al. designed an analog-to-information converter (AIC) based on CS, which is used to sample signal at an information rate that is much lower than Nyquist rate (Kirolos et al. 2006).

In Lv and Wu's CS based ultrasound imaging work, it is shown that the echo signal in time domain has a sparse representation and constructs basis functions based on waveforms. Also, it is utilized that AIC framework achieves sampling the echo signal with a low sampling rate and reconstructing the echo signal based on basis functions. Only 30% of data is used to implement ultrasound imaging without reducing the quality of image. The sampling rate of the raw data is 12 MHz normally, but the sampling rate 4 MHz is used in this method. The maximal error in amplitude is only about 2%.

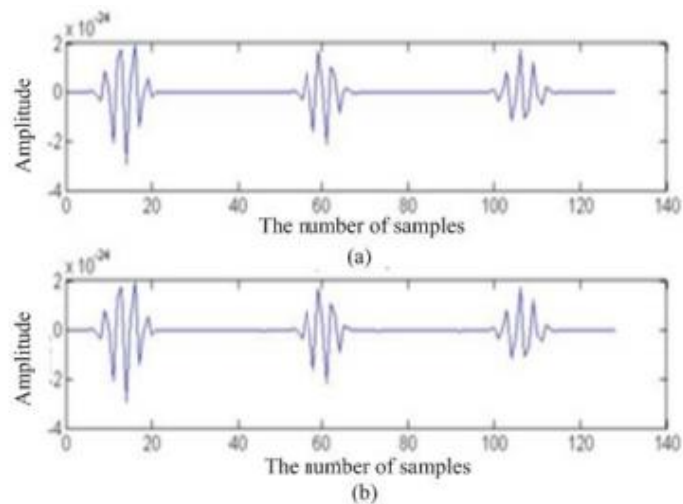


Figure 2.8 (a) The raw echo signal with sampling rate 12 MHz (b) The reconstructed signal with sampling rate 4 MHz (Lv and Wu, 2012).

Functional MRI (fMRI) has been considerably accepted as a standard tool to learn the function of brain. However, because of the limited resolution of MR scanning, researchers have experienced difficulties in various studies which usually require higher resolution.

In Jung and Ye's work, a new high spatio-temporal resolution fMRI technique based on compressed sensing theory is proposed. Functional MRI (fMRI) is a

technique to detect activated area in the brain by measuring the change of blood oxygen level-dependent (BOLD) contrast. However, since the change of BOLD signal is very small compared to full MR signal, scanning process must be quickly to prevent noisy signal due to subject motion or tissue pulsation.

The main contribution of this work is to apply compressed sensing based algorithm called k-t FOCUSS (Jung and Ye, 2009) to fMRI. To implement accelerated fMRI, 2-fold and 4-fold down sampled data are used and then the results are reconstructed by k-t FOCUSS. Thus high temporal resolution can be achieved through accelerated acquisition.

Also, Karhunen-Loeve transform (KLT) along temporal direction in k-t FOCUSS is used in this work and it outperforms other implementations in fMRI applications due to its adaptiveness of temporal variation. Unlike the Fourier transform, KL transform is a data dependent transform. The KLT is the optimal energy compaction transform and that most of the energy is compacted in a small number of coefficients, which is an ideal property for CS. k-t FOCUSS using KLT shows the best accuracy and better performance in both accelerations.

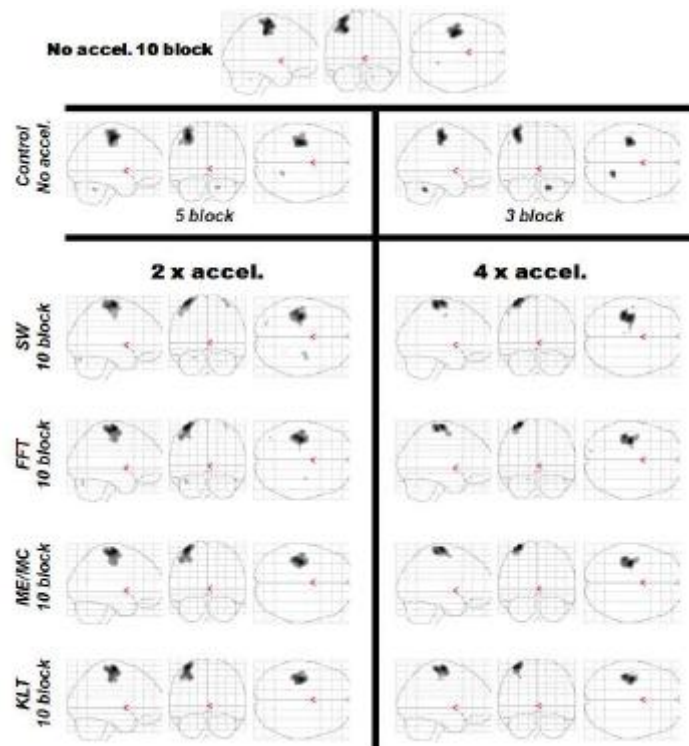


Figure 2.9 Activated brain areas for various methods and acceleration ratio. (SW: Sliding Window, ME/MC: Motion Estimation/Compensation) (Jung and Ye, 2009).

A media hash is a content-based representation of a digital multimedia signal. In Kang et al.'s work, the property of dimensionality reduction inherent in CS is used for image hash design. CS based hash size can be small and this method is computationally secure.

A robust and secure image hashing scheme via CS and visual information fidelity (VIF) exploits low-complexity hash extraction, it means that the hash can be simultaneously extracted while acquiring an image using the CS single-pixel imaging camera and short hash length, by means of coming from the highly sparse signal dimensionality reduction capability of CS.

An image quality assessment, called visual information fidelity (VIF), ranged from 0 to 1, is used. To quantify the visual quality of a distorted image, this is an image information measure that quantifies the information presented in its original version and how much of this information can be extracted from the distorted image. VIF models images in the wavelet domain which has been shown to be translation and rotation invariant.

For hash extraction, given an $m \times n$ sampling matrix Φ , controlled by a secret key S , x is randomly projected to a measurement vector with size M . For a received image x' to be authenticated, the same hash extraction process with the same key is applied. To compare two image hash vectors also the MSE between them is calculated besides VIF.

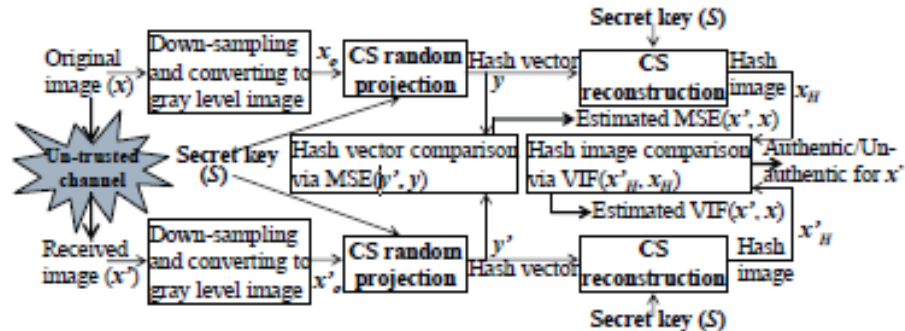


Figure 2.10 Hashing schema (Kang et al. 2009).

Some applications of compressed sensing are completely outside the area of imaging. One example is “analog to digital conversion,” a fundamental subject of wireless communications. For instance, the CDMA (Code Division Multiple Access) cell phone takes a voice message, which contains sound frequencies up to 4096 hertz, and spreads it out with hundreds of thousands of hertz. The signal is sparse because it contains only the information that is compressed using 4096 hertz. So a detector that uses compressed sensing can recover the signal more rapidly than a detector based on Shannon’s theorem (Mackenzie, 2009).

3 BRDF (Bidirectional Reflectance Distribution Function)

Real world materials have different reflection properties. Exact representation of the distribution of light reflected from the surface of a material has long been studied in computer graphics. Bidirectional Reflectance Distribution Function (BRDF) that is defined in terms of incoming and outgoing light directions is commonly used to describe such reflectance properties. BRDF is a function of four parameters: two parameters are for incoming light direction, two other parameters are for outgoing light direction.

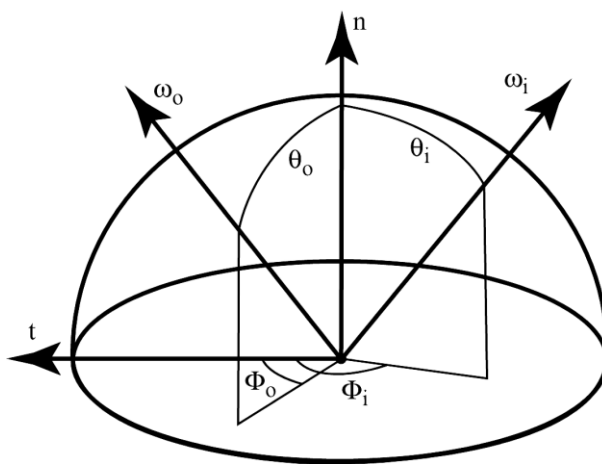


Figure 3.1 Four angles to describe a BRDF (Matusik et al. 2003).

a) Isotropic BRDFs

Isotropic BRDFs are used for materials for which rotations around surface normal makes no difference for BRDF reflectance values. In this case BRDF can be written as a function of three parameters. The parameters Φ_i and Φ_o can be replaced by one parameter $\Phi_{diff} = (\Phi_i - \Phi_o)$.

b) Anisotropic BRDFs

Anisotropic surfaces cannot be modeled using isotropic BRDFs. Brushed or burnished metals, hair or some fabrics are examples of anisotropic surfaces. Anisotropic surfaces have microgeometry with oriented elements. An observer usually doesn't see the microstructure, but instead see its effect on the reflected light.

3.1 Properties of BRDFs

a) Non-negativity

All values of a BRDF must be non-negative. In other words, they can be any value in the interval $(0, \infty)$.

b) Energy Conservation

The amount of energy that is received by the surface from some specific direction must be greater than the sum of the energy emitted by the surface to all possible directions.

c) Reciprocity

The surface reflectance should be independent of the direction of the light flow; it means that if the light direction is reversed the value of the BRDF should be the same.

3.2 Analytic reflectance models

Physically based analytic reflectance models or empirical analytic reflectance models generate the BRDFs used in computer graphics and computer vision. These BRDF models are only approximations of reflectance of real world materials. Also, most analytic reflectance models are successful for only particular subclasses of materials. These models have improved over the years to become more complex, consisting of more underlying physics (Matusik, 2003).

The well-known, simple and former reflectance model which shows the effects of specular reflection is the Phong model. For specular surfaces, this model assumes that incoming light tries to leave the surface on the direction of perfect reflection. Blinn develops a model that relies on the Phong model and since it uses the halfway direction it provides faster computation.

The Fresnel effect (increase in specularity at grazing angles) and the microscale geometry of a surface are necessary properties for BRDF modeling. Cook and Torrance, Torrance and Sparrow and Ashikhmin et al. have presented BRDF models based on surfaces made up of small planar microfacets. The Cook-Torrance and Torrance-Sparrow models are physically-based models. Only Ashikhmin et al. is an empirical model. These models have masking and self-shadowing effects. A comprehensive and computationally expensive model was developed by He et al., also Oren and Nayar presented a diffuse model to simulate rough and diffuse surfaces.

As opposed to the physically-based BRDF models, empirical models do not consider the physical basis of the light-material interaction. Ward develops an empirical model that has most important reflection concepts. His model adapts the basics of physical laws (like energy conservation and reciprocity) and it is relatively simple than most analytical reflectance models (Ward, 1992).

3.3 Fitting BRDF Data to Analytical Models

An alternative to analytic reflectance models is to directly measure values of the BRDF for different incoming and outgoing angles and then fit the measured data to a selected analytic model using various optimization techniques. There are some drawbacks to this measure-and-fit approach. First, measured values of the BRDF are usually not equal to the values of the analytic model. The measure-and-fit process is often operated by assuming that there is noise in the measurement process and that the fitting process filters out this noise. Second, the choice of the error function which the optimization process uses is very important. For example, error function based on the Euclidean distance is poor since it tends to overemphasize the specular peaks and ignore the off-specular reflection. Finally, there is no guarantee that the optimization process will do the best. Since most BRDF models are non-linear, the optimization phase used in the fitting process relies excessively on the initial guess for the model parameters. The quality of the initial guess can have an outstanding effect on the final parameter values of the model (Matusik, 2003).

3.4 BRDF Measurement

The third approach for reflectance modeling is to obtain dense measurements of reflectance and use these measurements directly as a BRDF. This method preserves the elaborateness of the reflectance function that is lost in a data-fitting approach. The classical device for measuring a BRDF is the gonio-reflectometer, which consists of a photometer and light source that are moved around a surface sample under computer control. Such devices measure a single radiance value at a time and this work makes this process very time-consuming. There have been attempts to make this acquisition process more productive by measuring many BRDF samples at once. This can be realized by using a digital camera and mirrors or spherical samples of the material. The method of using tabulated BRDFs becomes more expensive if the reflectance for all materials in a scene needs to be measured and stored. Also, since it is not a parameterized reflectance model, any change to the material property forces to finding a real material and acquiring its reflectance. The main advantage of these methods is they produce very realistic results, since acquired BRDFs come from real measured data (Matusik, 2003).

One of the most well-known BRDF database is the MERL MIT database. Data in the MERL MIT database have been acquired by Matusik et al. An image from Matusik et al.'s measurement system can be seen in Figure 3.2 The MERL MIT database consists of 100 different isotropic BRDF measurements (using $90 * 90 * 180 = 1\,458\,000$ measurements for each material) (Kurt, 2014). Materials in this library contain metals, paints, fabrics, minerals, synthetics, organic materials, and others. A data-driven approach is introduced for BRDF modeling. It interpolates/extrapolates new BRDFs from the sample BRDF data. With this approach, the produced BRDFs look very realistic since they are based on the measured BRDFs. Furthermore, a set of intuitive parameters are provided to allow users to change the properties of the output BRDF (Matusik et al. 2003).

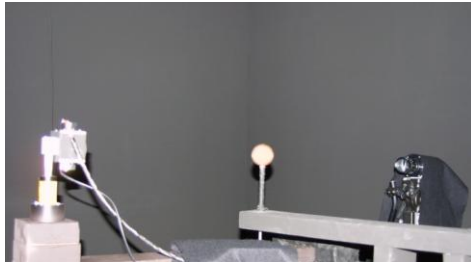


Figure 3.2 BRDF Measurement system of Matusik et al. The system is placed in a completely isolated room painted in black matte (Matusik et al., 2003).

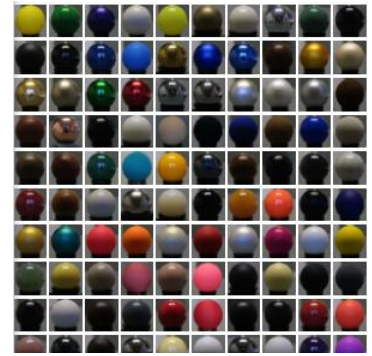


Figure 3.3 Pictures of the 100 acquired materials from Matusik BRDF Database (Matusik et al., 2003).

Dana et al. develop a system to measure BRDFs. Using a digital camera, a robot arm, and a light source, they obtain approximately 200 reflectance measurements with varying incident and reflected angles for each material sample. The data for about 61 materials is available as the CURET database (Figure 3.4). It has a relatively sparsely sampled BRDF.



Figure 3.4 CURET dataset (2007). 61 materials are used in BRDF measurements.

One of the first methods to accelerate the measurement process is found by Ward. His measurement device consists of a hemispherical mirror and a CCD camera with a fisheye lens. The most important advantage of his system is that the CCD camera can take multiple, simultaneous BRDF measurements. Each photosite of the imaging sensor includes a separate BRDF value. Measurement of BRDFs is carried

out by moving the light source and material over all incident angles. But, measurement of BRDF values near grazing angles is very difficult; so very specular BRDFs cannot be measured correctly.

Marschner et al. set up another known BRDF measurement system. The optical mirrors used by Ward and Dana to collect rays from different directions are replaced by two cameras, a light source, and a test sample. (Figure 3.5) Each point on the surface with a different surface normal represented a different BRDF measurement value. This system uses a spherical sample of isotropic material. A fixed camera took images of the sample under illumination with a rotating light source. The system, although set up for only isotropic BRDF measurements, it is fast and robust. Lu et al. use a similar imaging device with a cylindrical sample to measure the anisotropic BRDF of velvet (Matusik, 2003).

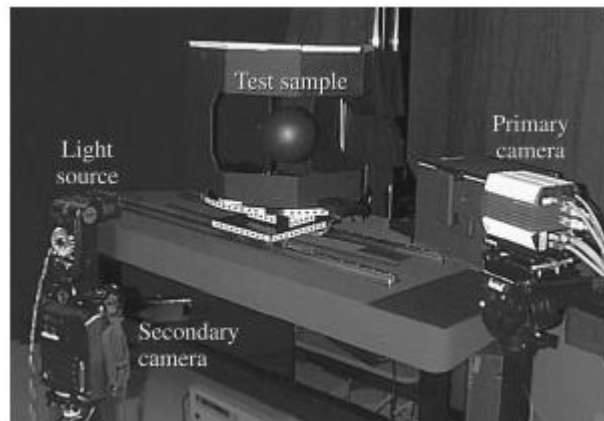


Figure 3.5 BRDF Measurement system of Marschner et al (Marschner et al. 2000).

3.5 Problems Associated with BRDF Measurements

Unfortunately, sufficient amount of BRDF data are difficult to obtain and measurements often have low angular resolution. On the other hand, the BRDF data obtained in this way is generally noisy and contains some missing values due to some difficulties in measuring BRDF near grazing angles (Rusinkiewicz, 1997). BRDF measuring systems suffer from occlusion problems because of using cameras, projectors and mirrors. In such cases, obtaining all BRDFs over a full hemisphere may not be possible and measurements taken at certain angles may be very noisy and

cannot be used for rendering. A solution for handling this problem may be ignoring the missing or highly noisy measurements and fit an analytical model to the remaining part of the data (Ngan et al. 2005).

In some other cases the optical elements of the system do not allow measurements at certain positions resulting considerable amount of missing data (Matusik et al. 2003). Experimental results have shown that approximately 60-70% of the measurements taken at grazing angles and 10-15% of the measurements at normal angles contain some errors (Lawrence, 2004). Furthermore, Romerio et. al. (2008) have mentioned about the existence of lens flare artifacts in BRDF measurements.

3.6 Reflectance Representations

The dense dimensionality of a BRDF, because of the desire to sample it at high resolutions, leads to sampling and storage problems. So, many researchers have searched for a more appropriate basis for representing BRDFs. As a result, various BRDF representations have been developed. Westin et al. proposed spherical harmonics to store their BRDF data. Schroeder et al. used spherical wavelets to represent a part of the BRDF. Lalonde and Fournier used wavelet decomposition process and wavelet coefficient trees to represent BRDFs. The main advantage of wavelets is that they allow performing local analysis. Other representations are Zernicke polynomials, separable approximations obtained using singular value decomposition and non-negative matrix factorization (Matusik, 2003). Empirical results have shown that these techniques can provide a correct and compact representation of BRDF data but do not offer an efficient importance sampling (Lawrence, 2004).

3.7 An Alternative Data Representation

The natural coordinate system $(\theta_i, \theta_o, \Phi_{diff})$ for isotropic BRDFs requires very dense angular sampling for representing specular peaks accurately (Matusik et al. 2003). Even when getting BRDF data at a dense grid (for example 1° spacing for each dimension), desired images cannot be get because of the specular highlights become an oval shape, oriented at different directions.

In order to prevent these sampling problems, a different coordinate system, introduced by Rusinkiewicz (1997) and illustrated in Figure 3.6 is used. This coordinate system is based on the half-angle (half-vector between incoming and outgoing directions) concept. The half-angle defines an ideal surface normal for which a mirror surface would reflect all of the incoming light in the specified outgoing direction. (Matusik, 2003).

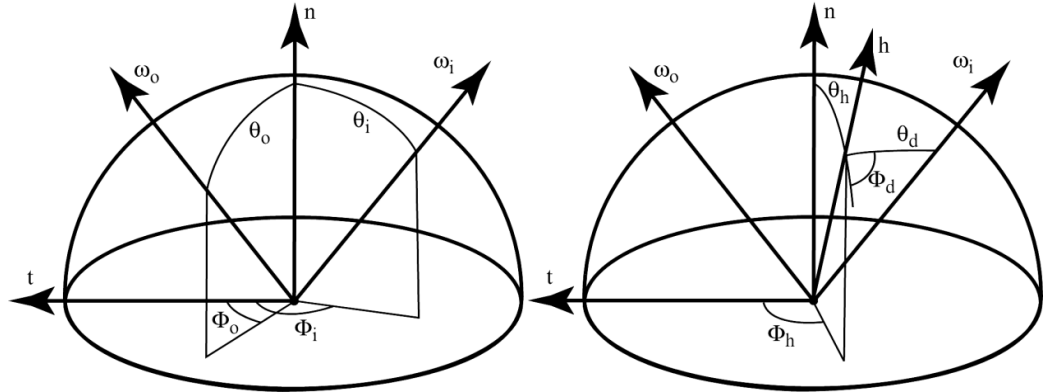


Figure 3.6 The standard coordinate system is shown on the left. Rusinkiewicz's coordinate system is shown on the right (Matusik et al. 2003).

Ngan et al. have validated that BRDF models, which include Fresnel term, can represent the measurements at grazing angles and normal incidence angles more accurately than other models (Ngan et al. 2005). For example, Ashikhmin-Shirley, Cook-Torrance and Kurt BRDF models contain Fresnel terms. So, these BRDF models usually give better results than Ward and Ward- Duer BRDF models which do not include any Fresnel term (Kurt, 2014).

Lawrence et al.'s BRDF representation uses a Non-negative Matrix Factorization based algorithm for compression and it's also appropriate for efficient BRDF importance sampling (2004). Öztürk et al.'s (2010) BRDF model is based on Rusinkiewicz coordinate system and uses Copula distributions. Bilgili et al.'s (2011) factored BRDF representation uses a Tucker-based factorization algorithm to represent measured BRDF data and it presents an efficient BRDF importance sampling. However, none of these data-driven BRDF representations can use noisy, sparse and irregular measurements successfully. So, these improper measurements

need to be preprocessed before they can be represented with a data-driven based representation (Kurt, 2014).



Figure 3.7 Rendered teapots using BRDFs from Matusik’s database: Nickel, hematite, gold paint and pink fabric (Matusik et al. 2003).

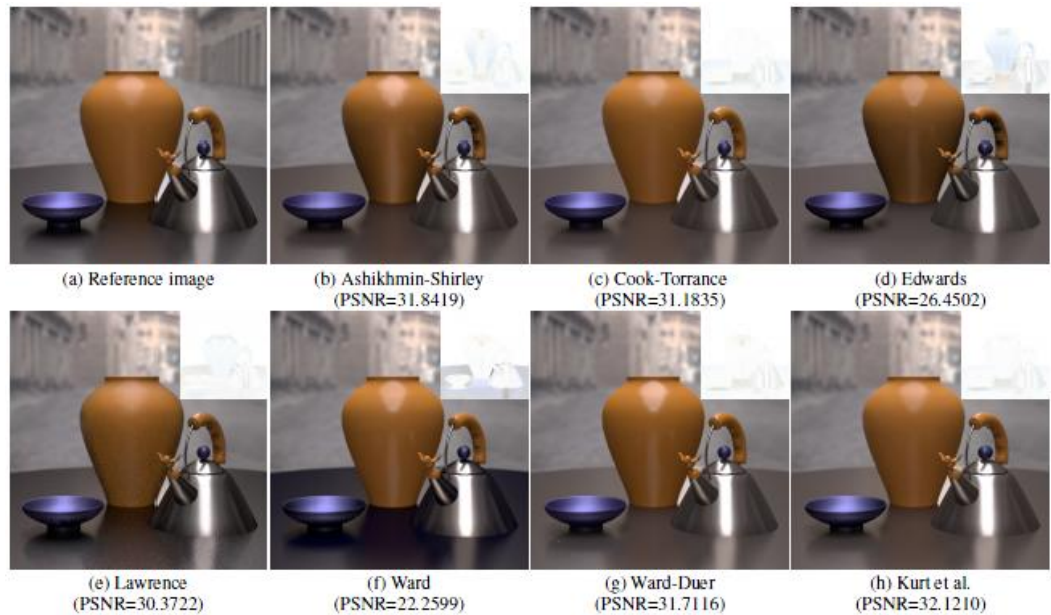


Figure 3.8 A visual and PSNR comparisons of some well-known BRDF representations on the Princeton scene (Kurt, 2014).



Figure 3.9 Based on BRDF modeling, photo-realistic renderings are generated for metallic car paint (Rump et al. 2008).

4 COMPRESSED SAMPLING AND BRDF DATA

In this work, it is showed that the Compressed Sampling technique can be used effectively for the data sets having some missing measurements. Also, it provides compression for large data sets. The BRDF data obtained is generally noisy and contains some missing observations due to some difficulties in measuring BRDF. Another major difficulty of using the BRDF data is its large size. These limitations prevent the direct use of the measured data (Matusik et al. 2003).

4.1 Reconstruction of Brdf Values

For the first trials, using fabric-pink material with parameters of a BRDF model (Blinn-Phong), within $0-2\pi$ interval 4000 values were calculated, then by using 30% of them, CS reconstruction process was realized. (For sampling matrix random permutation matrix and for basis matrix Fourier matrix were used) ($\text{norm}(\text{Original-Reconstructed})/\text{norm}(\text{Original}) = 3.0732e-006$)

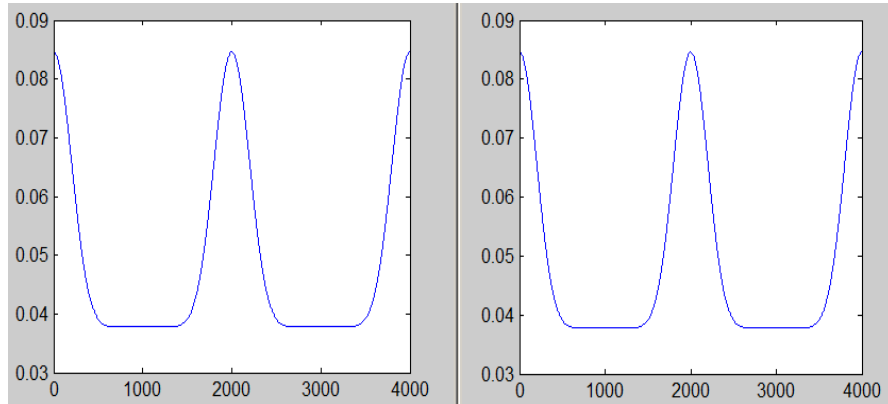


Figure 4.1 Left: Presentation of calculated BRDF values, Right: After CS reconstruction using 30% of BRDF values, acquired BRDF values.

In another trial, using dark-red-paint material, from its $90*90*180$ dimensional BRDF data, any $15*15*15$ dimensional data was taken, then by using 30% of them, CS reconstruction process was realized. (For sampling matrix random permutation matrix and for basis matrix Fourier matrix were used) ($\text{norm}(\text{Org-Rec})/\text{norm}(\text{Org}) = 0.0082$)

Essentially, the three dimensional data (from MERL database each with size 90 x 90 x 180) is divided into sub-sample blocks of size 15 x 15 x 15 and then it is vectorized into a one-dimensional vector. Random samples are generated from these sub-samples at a predefined sampling ratio.

A number of sampling methods have been proposed for reconstructing signal data (Candès et al. 2006). Unfortunately, these methods cannot be applied on BRDF data directly when the vector \mathbf{x} contains some missing data points, then the corresponding dot product between the rows of the Gaussian matrix Φ and \mathbf{x} cannot be determined.

By Gaussian matrix (for instance):

$$\mathbf{y} = \Phi \mathbf{x}$$

$$y = \begin{bmatrix} 0.15 & 0.23 & 1.87 & 0.39 \\ 0.98 & -0.63 & 1.38 & -0.18 \\ -1.12 & -0.21 & -0.69 & 0.48 \end{bmatrix} \begin{bmatrix} 1.5 \\ ? \\ 2.5 \\ 0.8 \end{bmatrix}$$

$$y = \begin{bmatrix} ? \\ ? \\ ? \end{bmatrix}$$
(4.1)

To overcome this difficulty, it is preferred using a different sampling procedure namely point sampling which is based on using a permutation matrix instead of a random Gaussian matrix.

By Permutation matrix (Point Sampling - for instance):

$$\mathbf{y} = \Phi \mathbf{x}$$

$$y = \begin{bmatrix} 1 & \mathbf{0} & 0 & 0 \\ 0 & \mathbf{0} & 0 & 1 \\ 0 & \mathbf{0} & 1 & 0 \end{bmatrix} \begin{bmatrix} 1.5 \\ ? \\ 2.5 \\ 0.8 \end{bmatrix}$$
(4.2)

$$y = \begin{bmatrix} 1.5 \\ 0.8 \\ 2.5 \end{bmatrix}$$

It is shown that the permutation matrices are coherent with the basis matrices which produce highly sparse data like the ones that are based on wavelets (Sen & Darabi, 2011). However, Fourier basis matrices are incoherent with permutation matrices. So, in this work, an $n \times n$ basis matrix Ψ is used whose entries are obtained through Fourier transforms.

The permutation matrix which consists of zeros and ones are provided by generating random numbers from a Bernoulli distribution for a specified probability. If a value of vector x is missing or negative, its corresponding column on the permutation matrix have all zero values. Thus, the matrix y doesn't become corrupted.

4.2 Reconstruction of Sampled Real BRDF Data

In this work, the non-linear optimization algorithm – SPGL1 (Van den Berg and Friedlander, 2011) is used for l_1 -norm optimization in reconstruction process.

To investigate the effect of the sampling ratio on the visual quality of the reconstructed images, random samples with ratios 1%, 2.5%, 5%, 10%, 25% and 50% are generated from six different materials namely dark-red-paint, green-fabric, blue-metallic-paint, gold-paint, fruitwood-241, chrome-steel are chosen. These materials are chosen to reflect the diffuse, glossy and specular properties of reflection.

Peak-Signal-to-Noise-Ratio (PSNR) values between original and reconstructed images are calculated for different sampling rates.

$$PSNR = 10 \log_{10} \left(\frac{R^2}{MSE} \right) \tag{4.3}$$

$R = 255$ for 8-bit data

$MSE =$ Mean Squared Error

Table 4.1 PSNR Results of Reconstruction of BRDF Data of Selected Six Materials

	1%	2.5%	5%	10%	25%	50%
Dark-red-paint	42.44	44.64	45.89	46.70	46.91	46.93
Green-fabric	44.89	48.29	48.85	49.20	49.34	49.34
Blue-metallic-paint	40.37	45.41	46.75	47.07	47.12	47.13
Gold-paint	40.51	43.41	44.62	45.24	45.40	45.38
Fruitwood-241	37.51	39.30	41.87	45.31	46.51	46.64
Chrome-steel	18.49	18.31	22.62	26.78	35.08	36.63

Original and reconstructed images and associated PSNR values for these six materials are seen in Appendix-1.

As it is seen in Table 4.1, 5% ratio is readily sufficient for diffuse and glossy materials on the average; but for specular materials especially for chrome-steel material, even 10% ratio is not sufficient. The reason of this situation is chrome-steel material's data has more irregular values and these irregular values cause lighting artifacts. This situation can be seen in Figure 4.2.

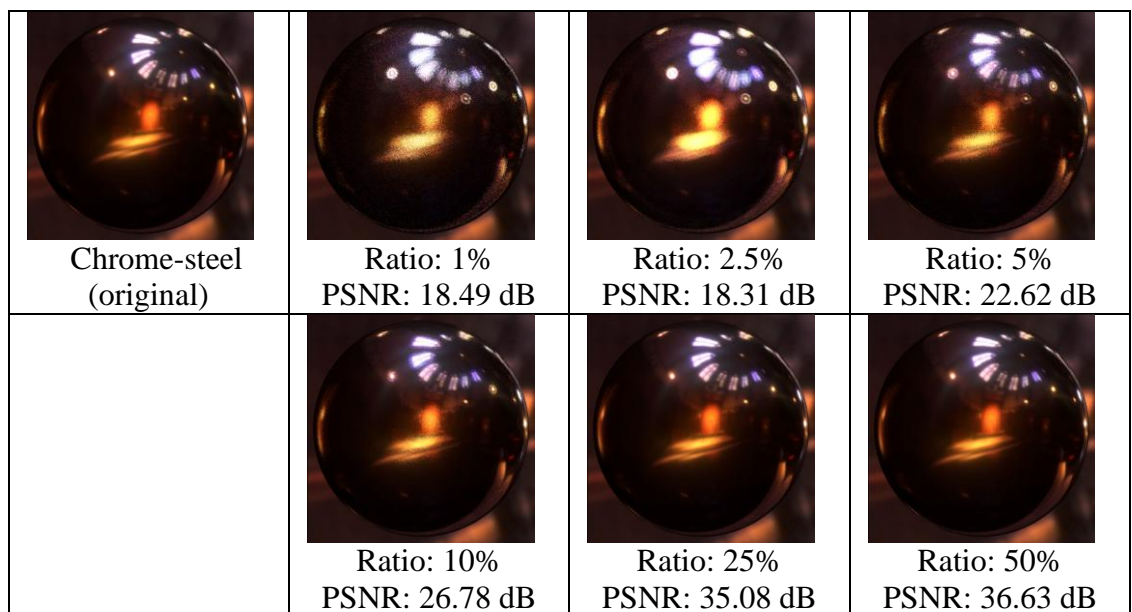


Figure 4.2 Results of various sampling ratios for chrome-steel material. Images have lighting artifacts even at 10% sampling ratio.

Some data sets contain irregular values as a result of certain measurement errors. To correct this situation, log transformation of the BRDF measurements is used to preserve the underlying property of BRDF data and straighten the irregular data values. After reconstruction the log transformation is reversed.

Table 4.2 PSNR Results of Reconstruction of BRDF Data of The Same Six Materials Using Log Transformation

	1%	2.5%	5%	10%	25%	50%
Dark-red-paint	45.04	49.54	51.46	52.33	52.48	52.91
Green-fabric	45.72	50.62	51.83	52.49	52.72	52.76
Blue-metallic-paint	41.58	47.58	51.71	52.51	52.62	52.64
Gold-paint	43.01	48.42	51.22	51.90	52.01	52.02
Fruitwood-241	41.68	44.73	50.26	51.82	52.11	52.15
Chrome-steel	26.92	35.36	43.20	47.20	48.86	48.99

As it is seen in Table 4.2 and Figure 4.3, using Log Transformation provides considerably successful results.

Original and reconstructed images and associated PSNR values Using Log Transformation for these six materials can be seen in Appendix-2.

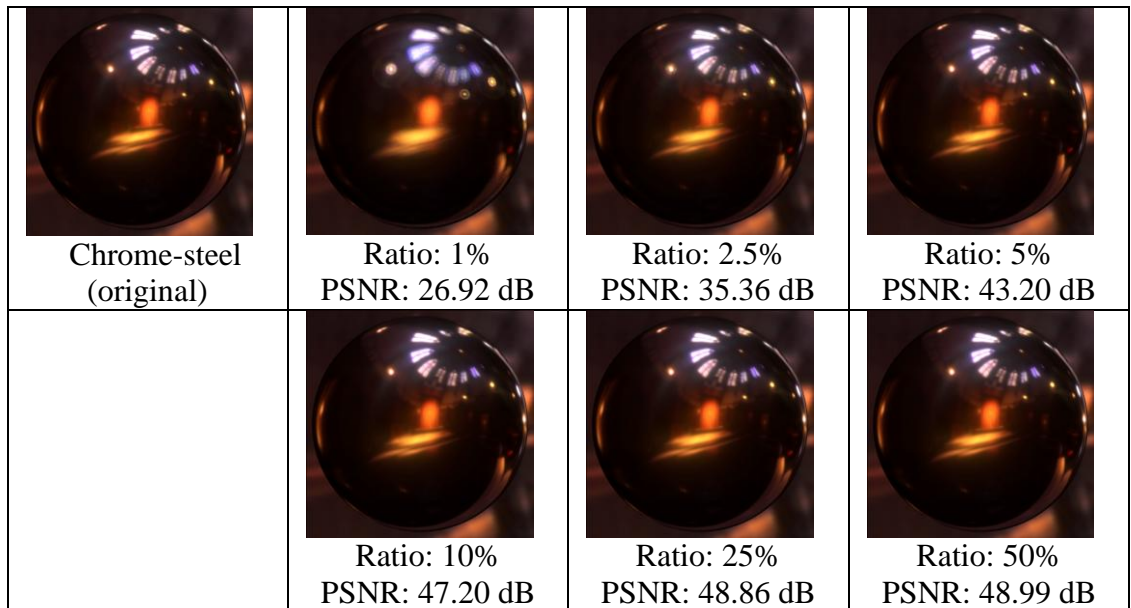


Figure 4.3 Results of various sampling ratios for chrome-steel material after using Log Transformation. Images don't have lighting artifacts beginning from 5% sampling ratio.

As it is seen in Table 4.2 and Figure 4.4, only 5% ratio is sufficient for all material types and PSNR values are above 40 dB. With log transformation, PSNR values are increased obviously. Therefore, log transformation method is used in all reconstructions after this.

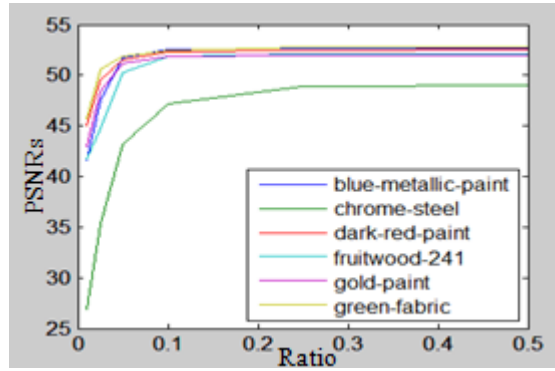


Figure 4.4 Above 0.05 ratio for all materials have sufficient PSNR values.

After all, for randomly selected 24 isotropic materials from MERL database using 5% of the BRDF measurements, data are reconstructed. PSNR values are given on Table 4.3 for each material.

Table 4.3 PSNR Results of Reconstruction of Using 5% of BRDF Data of 24 Sample Materials

	5%		5%
alum-bronze	46.54	hematite	45.51
aventurnine	47.52	ipswich-pine-221	50.65
beige-fabric	51.96	natural-209	49.78
black-obsidian	42.75	nylon	45.06
black-oxidized-steel	51.02	pearl-paint	51.51
black-soft-plastic	52.27	pickled-oak-260	51.58
blue-rubber	51.34	pink-jasper	48.89
cherry-235	51.14	polyethylene	46.31
colonial-maple -223	51.10	pure-rubber	51.95
delrin	48.63	pvc	48.59
gray-plastic	48.75	white-acrylic	49.04
green-acrylic	41.83	yellow-phenolic	49.76

Reconstructed images and difference images (in insets) and associated PSNR values for these 24 materials can be seen in Appendix-3. Insets indicate the differences between the reconstructed image and the corresponding original image.

After these successful PSNR results, to see the 2.5% ratio results for previous 24 materials and additional randomly selected 10 isotropic materials from MERL database, BRDF data are reconstructed and calculated PSNR values are given on Table 4.4 for each material.

Table 4.4 PSNR Results of Reconstruction of Using 2.5% and 5% of BRDF Data of 34 Sample Materials

	2.5%	5%		2.5%	5%
alum-bronze	38.68	46.54	pickled-oak-260	48.91	51.58
aventurnine	38.27	47.53	pink-jasper	41.96	48.89
black-obsidian	33.17	42.75	polyethylene	42.81	46.31
black-oxidized-steel	46.94	51.01	pure-rubber	49.61	51.95
black-soft-plastic	50.34	52.27	pvc	41.63	48.59
blue-rubber	47.71	51.34	white-acrylic	42.41	49.04
cherry-235	47.82	51.15	yellow-phenolic	42.91	49.76
colonial-maple -223	47.38	51.11	alumina-oxide	38.02	44.97
gray-plastic	42.78	48.77	aluminium	34.69	45.54
green-acrylic	35.45	41.83	brass	34.80	45.58
hematite	33.90	45.51	gold-metallic-paint2	39.37	47.75
delrin	44.62	48.63	green-latex	48.86	51.37
beige-fabric	49.22	51.96	green-plastic	37.33	47.22
ipswich-pine-221	46.28	50.66	nickel	37.75	47.09
natural-209	45.53	49.79	pink-fabric	49.53	51.92
nylon	41.11	45.06	red-metallic-paint	35.22	46.18
pearl-paint	47.90	51.50	violet-acrylic	37.79	47.12

Compressive sensing approach produces visually acceptable quality for all material types by sampling 5% of the original data. Also, for most of the materials – 26 in total 40 materials (especially diffuse and glossy materials) only 2.5% has sufficient PSNRs (over 40) and consequently adequate visual quality.

Original and reconstructed images acquired using 5% and 2.5% reconstruction ratios and associated PSNR values for these 34 materials can be seen in Appendix-4.

An example using 5% sampling ratio for two materials from MERL database is seen in Figure 4.5.

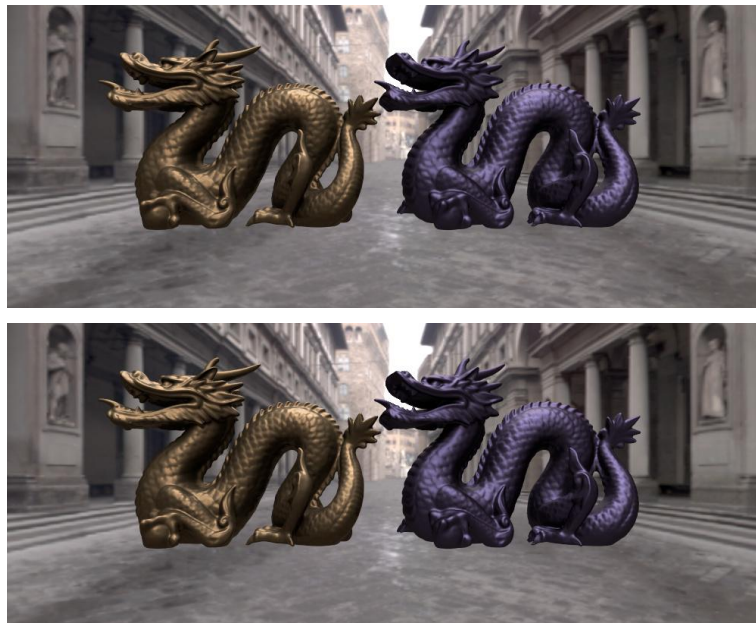


Figure 4.5 A sample scene has been rendered using alum-bronze and blue-metallic-paint materials. Top: Image based on the original data. Bottom: Image based on the reconstructed data using only 5% of the original data (PSNR is 51.63 dB).

5 CS AND BRDF DATA OF ANALYTIC REFLECTANCE MODELS

In both the fields of computer graphics and computer vision, surface reflectance has been approximated frequently with analytic reflectance models. These BRDF models produce similarities of reflectance of real materials. Also, most analytic reflectance models are usually limited to represent only particular subclasses of materials.

In this work, Ward and Cook-Torrance BRDF models that are extensively used are selected and BRDF data for various materials are constructed using these models respectively.

5.1 Ward Model

The Ward model is based on Gaussian distribution. It is simple and can be evaluated efficiently. Also it supports energy conservation and reciprocity properties of BRDF. The Ward model includes anisotropy, but it does not model Fresnel effects.

Common Notations	
N	normal
$V, (v_x, v_y, v_z)$	outgoing vector (view)
$L, (l_x, l_y, l_z)$	incoming vector (light)
R	mirror reflection of L
H	half vector
δ	angle between N and H

$$f_r(\theta_i, \phi_i, \theta_r, \phi_r) = \frac{k_d}{\pi} + k_s \frac{1}{\sqrt{(N \cdot L)(N \cdot V)}} \frac{\exp[-\tan^2 \delta / \alpha^2]}{4\pi\alpha^2}$$

where k_d is the diffuse reflectance coefficient; k_s is the specular reflectance coefficient; α is the standard deviation of surface slope.

5.2 Reconstruction of BRDF Data Obtained by Ward Model

For 40 materials that are selected previously, using their Ward parameters, BRDF values are calculated and filled in a 90*90*180 matrix. And then using only 2.5% of each data, BRDF data are reconstructed and calculated PSNR values are listed on Table 5.1 for each material. Only for 5 specular materials, PSNR values are a little bit low, so for these materials reconstruction process is realized again using 5% of data, PSNR values are on the same table.

Table 5.1 PSNR Results of Reconstruction of BRDF Data Obtained by Ward Analytic Model

	2.5%	5%		2.5%	5%
alum-bronze	45.85		pickled-oak-260	50.52	
aventurnine	44.41		pink-jasper	48.26	
black-obsidian	45.40		polyethylene	51.50	
black-oxidized-steel	49.71		pure-rubber	51.73	
black-soft-plastic	50.93		pvc	46.80	
blue-rubber	51.38		white-acrylic	49.26	
cherry-235	48.97		yellow-phenolic	47.26	
colonial-maple -223	49.36		alumina-oxide	46.83	
gray-plastic	47.71		aluminium	40.27	47.08
green-acrylic	45.64		brass	40.55	46.97
hematite	38.30	45.62	gold-metallic-paint2	46.10	
delrin	51.42		green-latex	52.18	
beige-fabric	52.22		green-plastic	44.44	
ipswich-pine-221	48.28		nickel	38.41	46.65
natural-209	47.17		pink-fabric	50.84	
nylon	50.74		red-metallic-paint	44.03	
pearl-paint	49.17		violet-acrylic	46.74	
blue-metallic-paint	48.60		chrome-steel	40.63	47.26
dark-red-paint	51.00		fruitwood-241	47.11	
gold-paint	44.86		green-fabric	52.07	

Reconstruction using Compressive sensing of BRDF Data obtained by Ward Analytic model produces visually acceptable quality and sufficient PSNR values for

approximately all material types by sampling only 2.5% of the original data. Also the results are better than the reconstructions of Matusik's Measured BRDF Data.

Original and reconstructed images acquired using 5% and 2.5% reconstruction ratios and associated PSNR values for these 40 materials can be seen in Appendix-5.

5.3 Cook-Torrance Model

According to the Cook-Torrance model, the surface is composed of tiny, perfectly reflective, smooth microfacets oriented at different directions. The facets are considered to be V-shaped. This model takes into account an average Fresnel term. The orientation of the facets has a distribution.

$$f_r(\theta_i, \phi_i, \theta_r, \phi_r) = \frac{k_d}{\pi} + \frac{k_s}{\pi} \frac{DG}{(N \cdot L)(N \cdot V)} \text{Fresnel}(F_0, V \cdot H)$$

where k_d , k_s are diffuse and specular reflectance coefficients; F is the Fresnel factor; D is the microfacet distribution function; and G is the geometrical attenuation factor.

5.4 Reconstruction of BRDF Data Obtained by Cook-Torrance Model

For 40 materials that are selected previously, using their Cook-Torrance parameters, BRDF values are calculated and filled in a 90*90*180 matrix. And then using only 2.5% of each data, BRDF data are reconstructed and calculated PSNR values are listed on Table 5.2 for each material. But for most materials, PSNR values are low (less than 40), so for all materials, reconstruction process is realized again using 5% of data, and then for 9 materials which PSNR values are low again, BRDF data is reconstructed using 10% of data and PSNR values are on the same table.

Table 5.2 PSNR Results of Reconstruction of BRDF Data Obtained by Cook-Torrance Analytic Model

	2.5%	5%	10%		2.5%	5%	10%
alum-bronze	33.53	39.39	43.81	pickled-oak-260	38.93	46.12	
aventurnine	32.37	41.96		pink-jasper	34.58	42.76	
black-obsidian	32.17	44.45		polyethylene	39.62	49.04	
black-oxidized-steel	32.76	44.46		pure-rubber	38.77	48.64	
black-soft-plastic	35.84	47.53		pvc	32.52	37.19	44.46
blue-rubber	34.83	45.95		white-acrylic	35.55	40.97	
cherry-235	31.16	41.94		yellow-phenolic	34.33	43.80	
colonial-maple-223	31.35	40.68		alumina-oxide	37.93	39.39	42.71
gray-plastic	32.85	42.75		aluminium	32.85	36.89	45.04
green-acrylic	33.70	40.10		brass	31.87	34.96	44.74
hematite	30.54	33.74	45.35	gold-metallic-paint2	33.05	42.14	
delrin	34.78	44.47		green-latex	42.29	50.53	
beige-fabric	41.79	50.84		green-plastic	36.98	39.87	44.51
ipswich-pine-221	30.12	41.19		nickel	32.12	38.12	44.98
natural-209	30.92	40.77		pink-fabric	42.22	49.23	
nylon	35.00	42.16		red-metallic-paint	33.98	42.67	
pearl-paint	36.50	45.96		violet-acrylic	33.25	42.48	
blue-metallic-paint	34.51	46.00		chrome-steel	32.10	36.58	45.43
dark-red-paint	38.28	47.41		fruitwood-241	30.46	41.93	
gold-paint	35.53	44.68		green-fabric	36.89	49.39	

Reconstruction of BRDF Data obtained by Cook-Torrance Analytic model with 2.5%, for most materials, PSNR values are low. But 5% ratio produces visually acceptable quality and sufficient PSNR values for most materials. Only for 9 materials which PSNR values are low with 5%, BRDF data is reconstructed using 10% of data. PSNR results are good for these 9 specular materials with 10% ratio.

Original and reconstructed images acquired using 2.5%, 5% and 10% reconstruction ratios and associated PSNR values for these 40 materials can be seen in Appendix-6.

6 CONCLUSION

In this work, the use of Compressed Sampling technique to realize a procedure for processing large BRDF data is analyzed. In data reconstruction, Compressive Sampling can be more efficient than traditional sampling when data is sparse. Considering the fact that the BRDF data often can be highly sparse, it can be reconstructed efficiently using Compressed Sampling technique. It is proved that the proposed technique can also be used for the data sets having some missing or unreliable measurements. Using BRDF measurements of numerous isotropic materials, it is shown that high quality images can be reconstructed and high PSNR values can be obtained at very low sampling ratios for both diffuse and glossy materials. Similar results also are obtained for the specular materials at slightly higher sampling ratios.

Also in this work, using Ward and Cook-Torrance BRDF models, BRDF data are acquired for various materials using these models respectively. Reconstruction using Compressed sampling of BRDF Data obtained by Ward Analytic model produces visually acceptable quality and sufficient PSNR values for approximately all material types by sampling only 2.5% of the original data. Reconstruction of BRDF Data obtained by Cook-Torrance Analytic model with 2.5%, for most materials, PSNR values are low. But 5% ratio produces visually acceptable quality and sufficient PSNR values for most materials.

Modeling and representation of anisotropic data is difficult. Much more data acquisition is needed for this case as compared with isotropic materials. The proposed approach can be extended to BRDF reconstruction of images for anisotropic materials later on.

In this thesis work, applications are developed in Matlab application development environment and using script language of Matlab.

REFERENCES

Baraniuk, R., 2007, Compressive sensing. IEEE Signal Processing Mag, pages 118 – 120.

Bilgili, A., Öztürk, A., and Kurt, M., 2011, A general BRDF representation based on tensor decomposition, Computer Graphics Forum 30, 8, 2427–2439.

Candès, E.J., 2006, Compressive Sampling, Proceedings of the International Congress of Mathematicians, Madrid, Spain.

Candès, E.J., Romberg, J., Tao, T., 2006, Robust Uncertainty Principles: Exact Signal Reconstruction from Highly Incomplete Frequency Information. IEEE Trans. on Information Theory, 52(2) pp. 489 - 509, February 2006.

Candès, E.J., Wakin, B., 2008, An Introduction To Compressive Sampling, IEEE Signal Processing Magazine, March 2008, 21-30.

CUReT, 2007, Columbia-Utrecht Reflectance and Texture Database, <http://www1.cs.columbia.edu/CAVE/software/curet/index.php>

Donoho, D., 2004, Compressed sensing, Preprint.

<https://www.math.ucdavis.edu/~mpf/spgl1/index.html>

Jung, H., Ye, J.C., 2009, Performance evaluation of accelerated functional MRI acquisition using compressed sensing, Biomedical Imaging: From Nano to Macro, 2009. ISBI '09. IEEE International Symposium.

Jung, H., Sung, K., Nayak, K.S., Kim, E.Y., Ye, J.C., 2009, k-t FOCUSS: A general compressed sensing framework for high resolution dynamic mri, Magnetic Resonance in Medicine, vol. 61, pp. 103–116, Jan 2009.

Kang, L., Lu, C., Hsu, C., 2009, Compressive Sensing-Based Image Hashing, Image Processing (ICIP), 2009 16th IEEE International Conference.

REFERENCES (continue)

Kirolos, S., Laska, J., Wakin, M., et al., 2006, Analog-to-information conversion via random demodulation, pp. 71-74.

Kurt, M., 2014, Grand Challenges in BSDF Measurement and Modeling, The Workshop on Light Redirection and Scatter: Measurement, Modeling, Simulation, Lucerne, Switzerland (Invited Talk).

Lawrence, J., Rusinkiewicz, S., and Ramamoorthi, R., 2004, Efficient BRDF importance sampling using a factored representation. *ACM Trans. Graph.*, 23(3):496–505.

Lee, I., 2011, Weighted Measurement Reuse for Compressive Video Sensing Reconstruction, Image and vision computing New Zealand (IVCNZ 2011), Invalid Code, 277-281.

Lv, Y., Wu, W., 2012, Compressive Ultrasound Imaging Based on Analog to Information Conversion, Biomedical Engineering and Biotechnology (iCBEB), 2012 International Conference.

Mackenzie, D., 2009, Compressed Sensing Makes Every Pixel Count, "Compressed sensing makes every pixel count", What's Happening in the Math. Sciences, AMS, 114-127.

Marschner, S.R., Westin, S.H., Lafortune, E.P.F., and Torrance, K.E., 2000, Image-based bidirectional reflectance distribution function measurement, *APPLIED OPTICS* Vol. 39, No. 16.

Matusik, W., 2003, PHD thesis.

Matusik, W., Pfister, H., Brand, M., and McMillan, L., 2003, A data-driven reflectance model. *ACM Trans. Graph.*, 22(3):759–769.

REFERENCES (continue)

Matusik, W., Pfister, H., Brand, M., and McMillan, L., 2003, Efficient isotropic BRDF measurement. In Proceedings of the 14th Eurographics workshop on Rendering, EGRW'03, pages 241–247, Aire-la-Ville, Switzerland, Eurographics Association.

Matusik, W., Pfister, H., Brand, M., and McMillan, L., Merl BRDF database. <http://www.merl.com/brdf/>.

Needell, D., Vershynin, R., 2007, Uniform uncertainty principle and signal recovery via regularized orthogonal matching pursuit, preprint.

Ngan, A., Durand, F., and Matusik, W., 2005, Experimental analysis of brdf models. In Proceedings of the Eurographics Symposium on Rendering, pages 117–226. Eurographics Association.

Öztürk, A., Kurt, M., and Bilgili, A., 2010, A copula-based brdf model, Computer Graphics Forum 29, 6 (September), 1795–1806.

Romberg, J., 2008, Imaging via Compressive Sampling, IEEE Signal Processing Magazine, March 2008, 14-20.

Romeiro, F., Vasilyev, Y., Zickler, T., 2008, Passive reflectometry. In David A. Forsyth, Philip H. S. Torr, and Andrew Zisserman, editors, ECCV (4), volume 5305 of Lecture Notes in Computer Science, pages 859–872. Springer.

Rump, M., Muller, G., Scarlette, R., Koch, D., Klein, R., 2008, Photo-realistic Rendering of Metallic Car Paint from Image-Based Measurements, Computer Graphics Forum 2008; 27(2): 527-536.

Rusinkiewicz, S., 1997, A survey of BRDF representation for computer graphics. CS348c. Universidad de Standford.

REFERENCES (continue)

Sen, P., Darabi, S., 2009, A Novel Framework For Imaging Using Compressed Sensing. Image Processing (ICIP), 16th IEEE International Conference.

Sen, P., Darabi, S., 2009, Compressive Image Super-resolution. Asilomar'09 Proceedings of the 43rd Asilomar Conference on Signals, Systems and Computers.

Seylan, N., Ergun, S., Öztürk, A., 2013, BRDF Reconstruction Using Compressive Sensing. WSCG International Conference on Computer Graphics, Visualization and Computer Vision, pp. 88-94.

Tropp, J.A., Gilbert, A.C., 2007, Signal recovery from random measurements via orthogonal matching pursuit, IEEE Trans. on Information Theory, vol. 53, no. 12, pp. 4655–4666, Dec. 2007.

Van den Berg, E., and Friedlander, M. P., 2011, Sparse optimization with least-squares constraints SIAM J. on Optimization, 21(4):1201–1229.

Wakin, M.B., Laska, J.N., Duarte, M.F., Baron, D., 2006, An Architecture for Compressive Imaging, Image Processing, 2006 IEEE International Conference.

Ward, G.J., 1992, Measuring And Modeling Anisotropic Reflection. SIGGRAPH Computer Graphics, Vol. 26, Issue 2, pp. 265-272.

APPENDICES

APPENDIX – 1 Original and reconstructed images and associated PSNR values for selected six materials

APPENDIX – 2 Original and reconstructed images and associated PSNR values Using LogTransformation for selected six materials

APPENDIX – 3 Reconstructed images and difference images (in insets) and associated PSNR values for selected 24 materials and for 5% sampling ratio

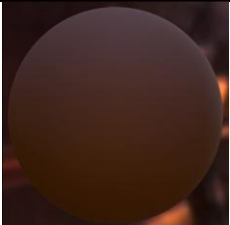
APPENDIX – 4 Original and reconstructed images acquired using 5% and 2.5% reconstruction ratios and associated PSNR values for 34 materials

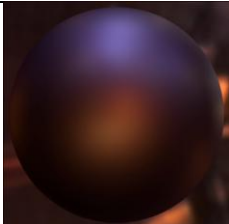
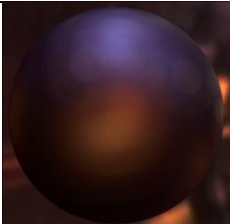
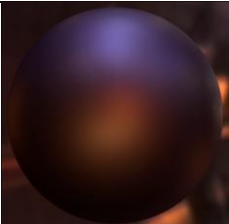
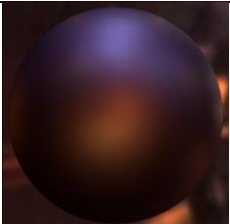
APPENDIX – 5 Results of Reconstruction of BRDF Data Obtained by Ward Model

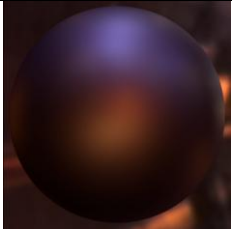
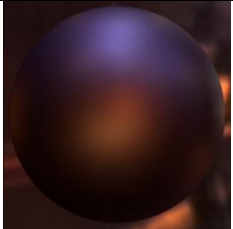
APPENDIX – 6 Results of Reconstruction of BRDF Data Obtained by Cook-Torrance Model

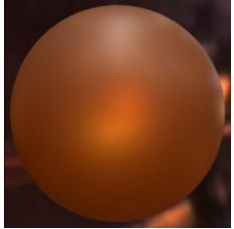
APPENDIX – 1 Original and reconstructed images and associated PSNR values for selected six materials

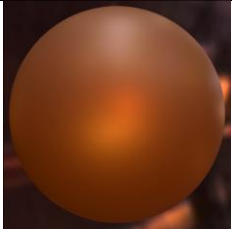
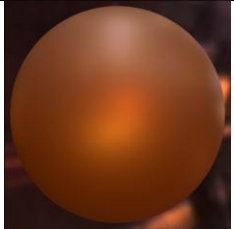
			
Dark-red-paint (original)	Ratio: 1% PSNR: 42.44 dB	Ratio: 2.5% PSNR: 44.64 dB	Ratio: 5% PSNR: 45.89 dB
			
	Ratio: 10% PSNR: 46.70 dB	Ratio: 25% PSNR: 46.91 dB	Ratio: 50% PSNR: 46.93 dB

			
Green-fabric (original)	Ratio: 1% PSNR: 44.89 dB	Ratio: 2.5% PSNR: 48.29 dB	Ratio: 5% PSNR: 48.85 dB
			
	Ratio: 10% PSNR: 49.20 dB	Ratio: 25% PSNR: 49.34 dB	Ratio: 50% PSNR: 49.34 dB

			
Blue-metallic-paint (original)	Ratio: 1% PSNR: 40.37 dB	Ratio: 2.5% PSNR: 45.41 dB	Ratio: 5% PSNR: 46.75 dB

	 Ratio: 10% PSNR: 47.07 dB	 Ratio: 25% PSNR: 47.12 dB	 Ratio: 50% PSNR: 47.13 dB
--	---	--	---

 Gold-paint (original)	 Ratio: 1% PSNR: 40.51 dB	 Ratio: 2.5% PSNR: 43.41 dB	 Ratio: 5% PSNR: 44.62 dB
---	--	---	--

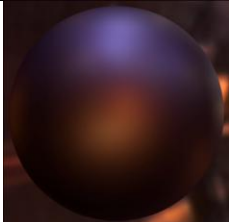
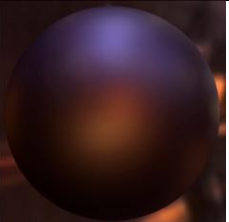
	 Ratio: 10% PSNR: 45.24 dB	 Ratio: 25% PSNR: 45.40 dB	 Ratio: 50% PSNR: 45.38 dB
--	--	---	--

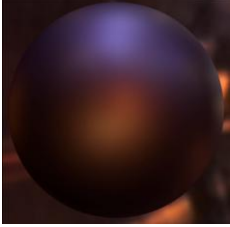
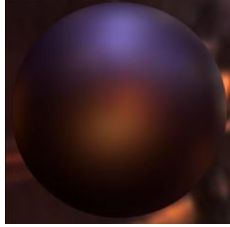
 Fruitwood-241 (original)	 Ratio: 1% PSNR: 37.51 dB	 Ratio: 2.5% PSNR: 39.30 dB	 Ratio: 5% PSNR: 41.87 dB
--	--	---	--

	 Ratio: 10% PSNR: 45.31 dB	 Ratio: 25% PSNR: 46.51 dB	 Ratio: 50% PSNR: 46.64 dB
--	---	--	---

 <p>Chrome-steel (original)</p>	 <p>Ratio: 1% PSNR: 18.49 dB</p>	 <p>Ratio: 2.5% PSNR: 18.31 dB</p>	 <p>Ratio: 5% PSNR: 22.62 dB</p>
	 <p>Ratio: 10% PSNR: 26.78 dB</p>	 <p>Ratio: 25% PSNR: 35.08 dB</p>	 <p>Ratio: 50% PSNR: 36.63 dB</p>

APPENDIX – 2 Original and reconstructed images and associated PSNR values
Using LogTransformation for selected six materials

 Dark-red-paint (original)	 Ratio: 1% PSNR: 45.04 dB	 Ratio: 2.5% PSNR: 49.54 dB	 Ratio: 5% PSNR: 51.46 dB
	 Ratio: 10% PSNR: 52.33 dB	 Ratio: 25% PSNR: 52.48 dB	 Ratio: 50% PSNR: 52.91 dB
 Green-fabric (original)	 Ratio: 1% PSNR: 45.72 dB	 Ratio: 2.5% PSNR: 50.62 dB	 Ratio: 5% PSNR: 51.83 dB
	 Ratio: 10% PSNR: 52.49 dB	 Ratio: 25% PSNR: 52.72 dB	 Ratio: 50% PSNR: 52.76 dB
 Blue-metallic-paint (original)	 Ratio: 1% PSNR: 41.58 dB	 Ratio: 2.5% PSNR: 47.58 dB	 Ratio: 5% PSNR: 51.71 dB

	 Ratio: 10% PSNR: 52.51 dB	 Ratio: 25% PSNR: 52.62 dB	 Ratio: 50% PSNR: 52.64 dB
--	---	--	---

 Gold-paint (original)	 Ratio: 1% PSNR: 43.01 dB	 Ratio: 2.5% PSNR: 48.42 dB	 Ratio: 5% PSNR: 51.22 dB
---	--	---	--

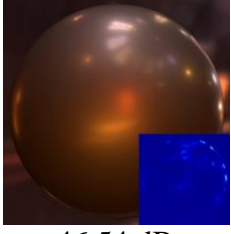
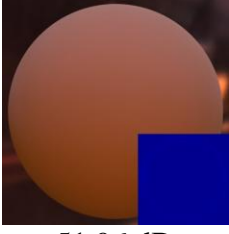
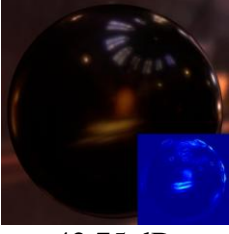
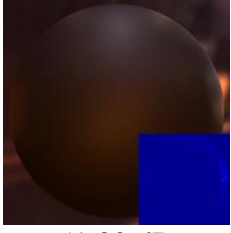
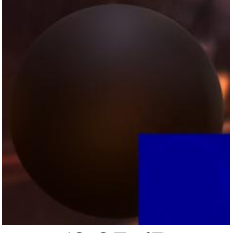
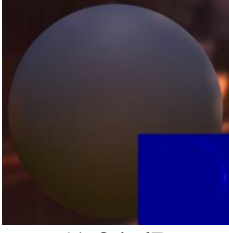
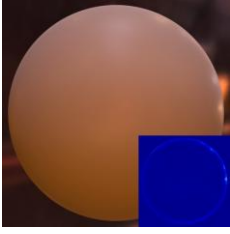
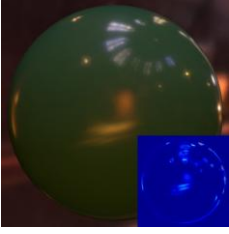
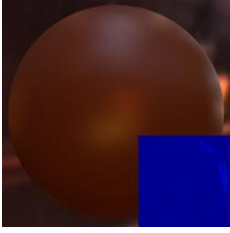
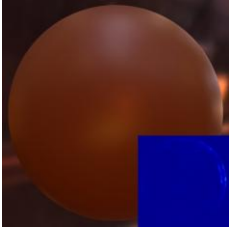
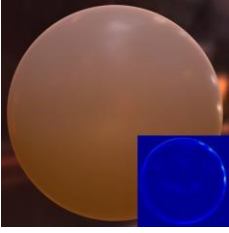
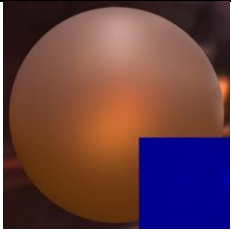
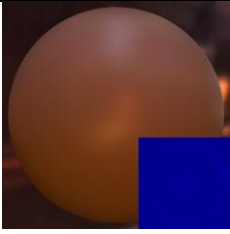
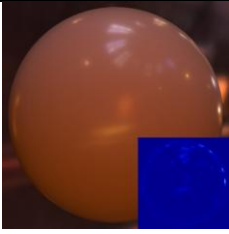
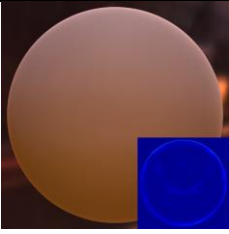
	 Ratio: 10% PSNR: 51.90 dB	 Ratio: 25% PSNR: 52.01 dB	 Ratio: 50% PSNR: 52.02 dB
--	--	---	--

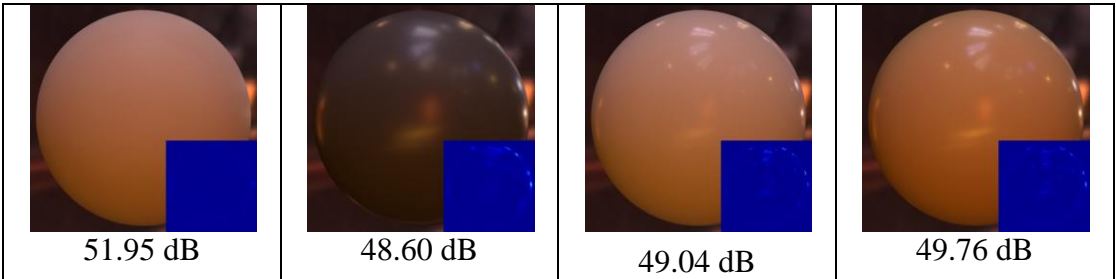
 Fruitwood-241 (original)	 Ratio: 1% PSNR: 41.68 dB	 Ratio: 2.5% PSNR: 44.73 dB	 Ratio: 5% PSNR: 50.26 dB
--	--	---	--

	 Ratio: 10% PSNR: 51.82 dB	 Ratio: 25% PSNR: 52.11 dB	 Ratio: 50% PSNR: 52.15 dB
--	---	--	---

 <p>Chrome-steel (original)</p>	 <p>Ratio: 1% PSNR: 26.92 dB</p>	 <p>Ratio: 2.5% PSNR: 35.36 dB</p>	 <p>Ratio: 5% PSNR: 43.20 dB</p>
	 <p>Ratio: 10% PSNR: 47.20 dB</p>	 <p>Ratio: 25% PSNR: 48.86 dB</p>	 <p>Ratio: 50% PSNR: 48.99 dB</p>

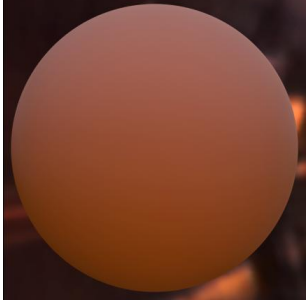
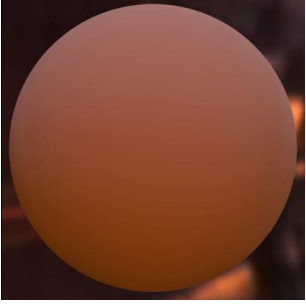
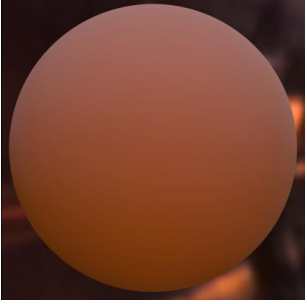
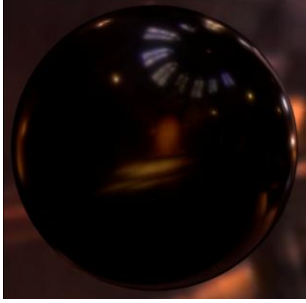
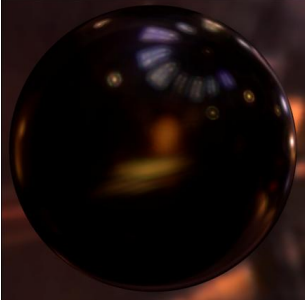
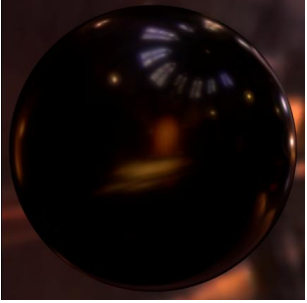
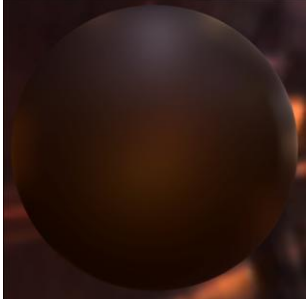
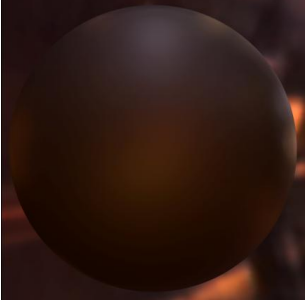
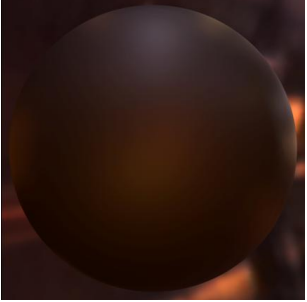
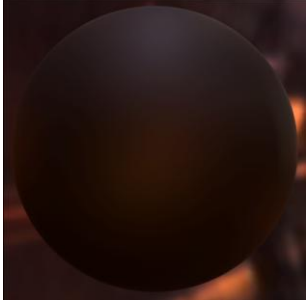
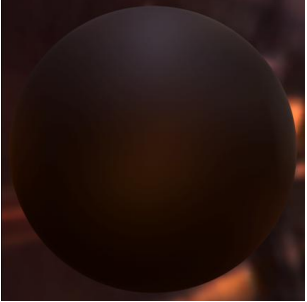
APPENDIX – 3 Reconstructed images and difference images (in insets) and associated PSNR values for selected 24 materials and for 5% sampling ratio

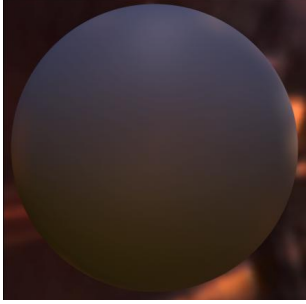
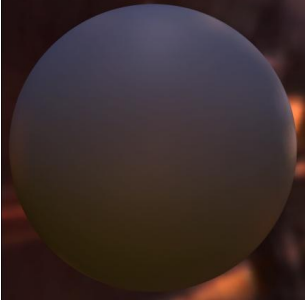
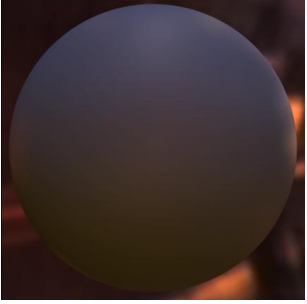
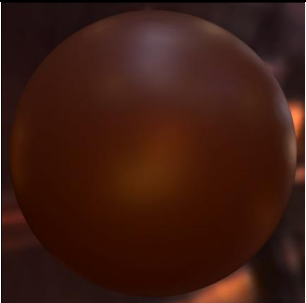
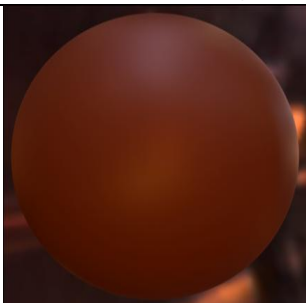
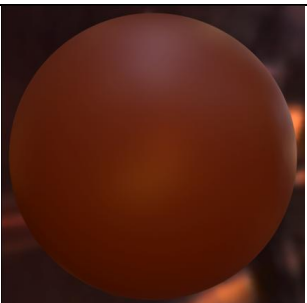
 46.54 dB	 47.52 dB	 51.96 dB	 42.75 dB
 51.02 dB	 52.27 dB	 51.34 dB	 51.14 dB
 51.10 dB	 48.63 dB	 48.75 dB	 41.83 dB
 45.51 dB	 50.65 dB	 49.78 dB	 45.06 dB
 51.51 dB	 51.58 dB	 48.90 dB	 46.31 dB

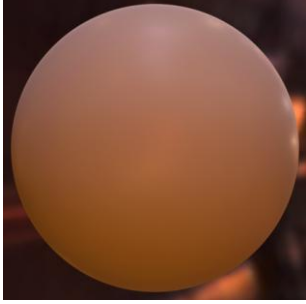
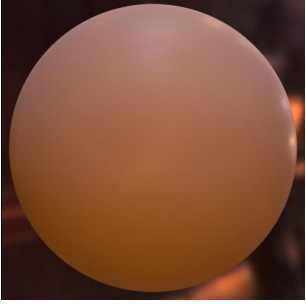
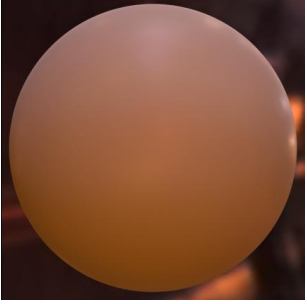
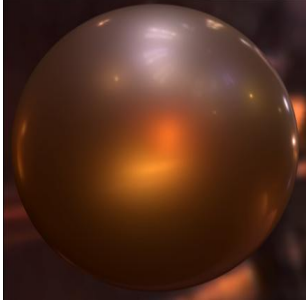
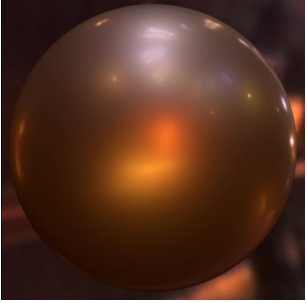
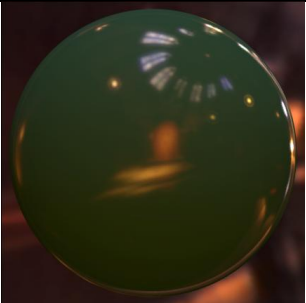


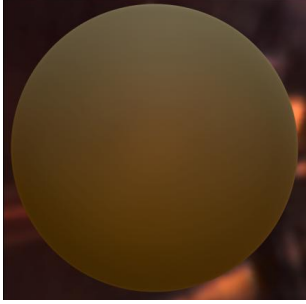
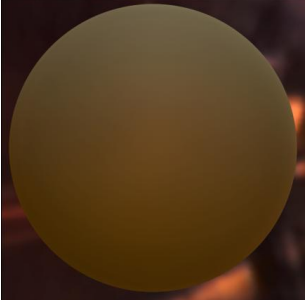
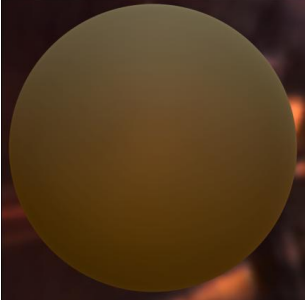
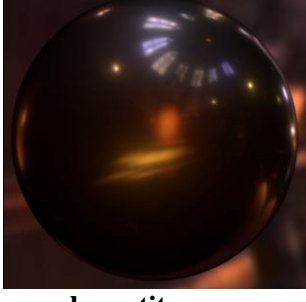
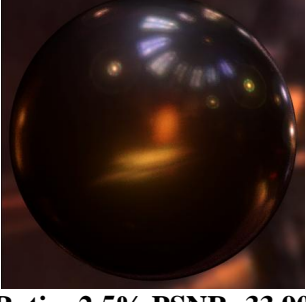
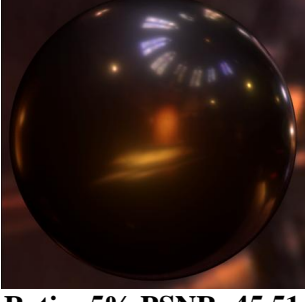
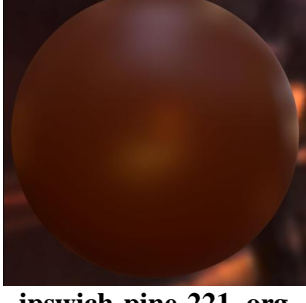
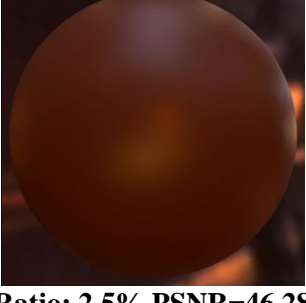
APPENDIX – 4 Original and reconstructed images acquired using 5% and 2.5% reconstruction ratios and associated PSNR values for 34 materials

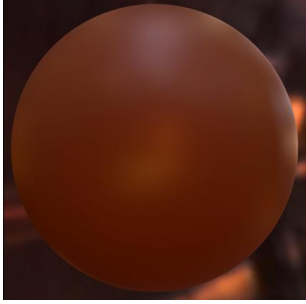
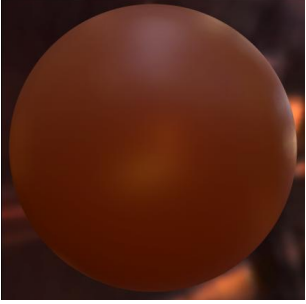
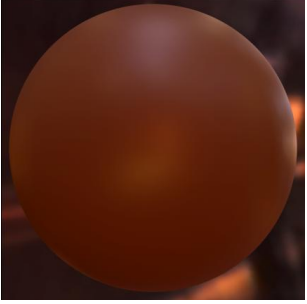
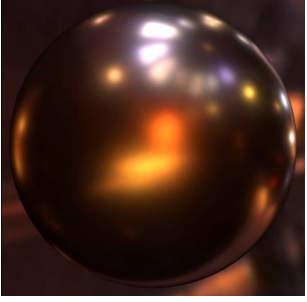
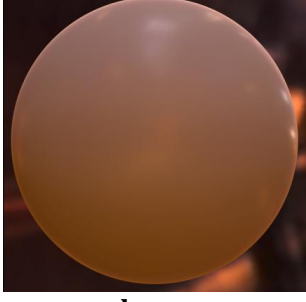
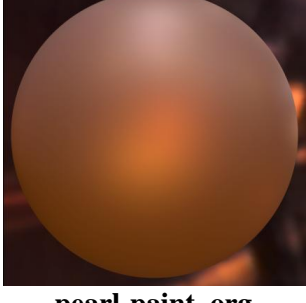
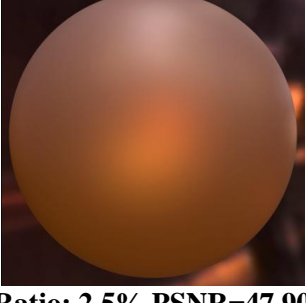
 alum-bronze_org	 Ratio: 2.5% PSNR=38.68	 Ratio: 5% PSNR=46.54
 alumina-oxide_org	 Ratio: 2.5% PSNR=38.02	 Ratio: 5% PSNR=44.97
 aluminium_org	 Ratio: 2.5% PSNR=34.69	 Ratio: 5% PSNR=45.54
 aventurnine_org	 Ratio: 2.5% PSNR=38.27	 Ratio: 5% PSNR=47.53

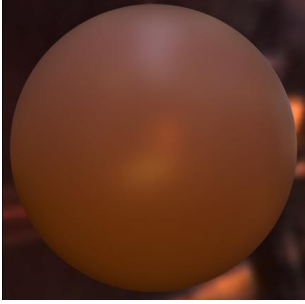
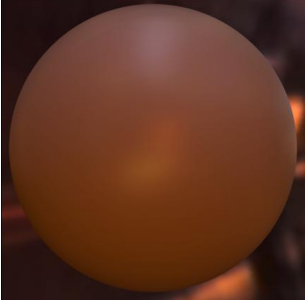
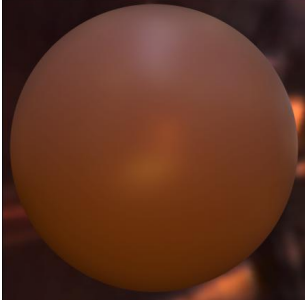
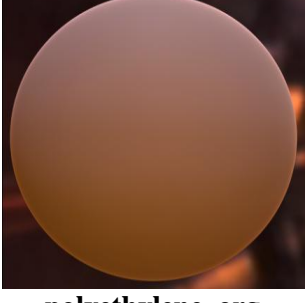
		
beige-fabric_org	Ratio: 2.5% PSNR=49.22	Ratio: 5% PSNR=51.96
		
black-obsidian_org	Ratio: 2.5% PSNR=33.17	Ratio: 5% PSNR=42.75
		
black-oxidized-steel_org	Ratio: 2.5% PSNR=46.94	Ratio: 5% PSNR=51.01
		
black-soft-plastic_org	Ratio: 2.5% PSNR=50.34	Ratio: 5% PSNR=52.27

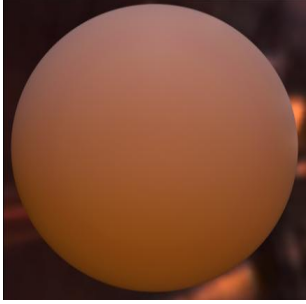
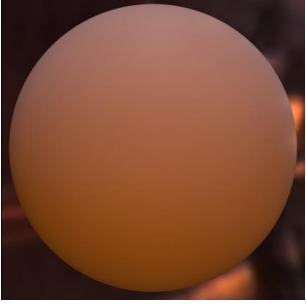
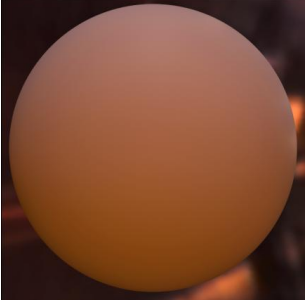
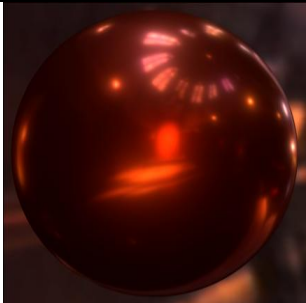
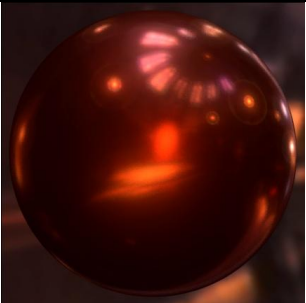
		
blue-rubber_org	Ratio: 2.5% PSNR=47.71	Ratio: 5% PSNR=51.34
		
brass_org	Ratio: 2.5% PSNR=34.80	Ratio: 5% PSNR=45.58
		
cherry-235_org	Ratio: 2.5% PSNR=47.82	Ratio: 5% PSNR=51.15
		
colonial-maple-223_org	Ratio: 2.5% PSNR=47.38	Ratio: 5% PSNR=51.11

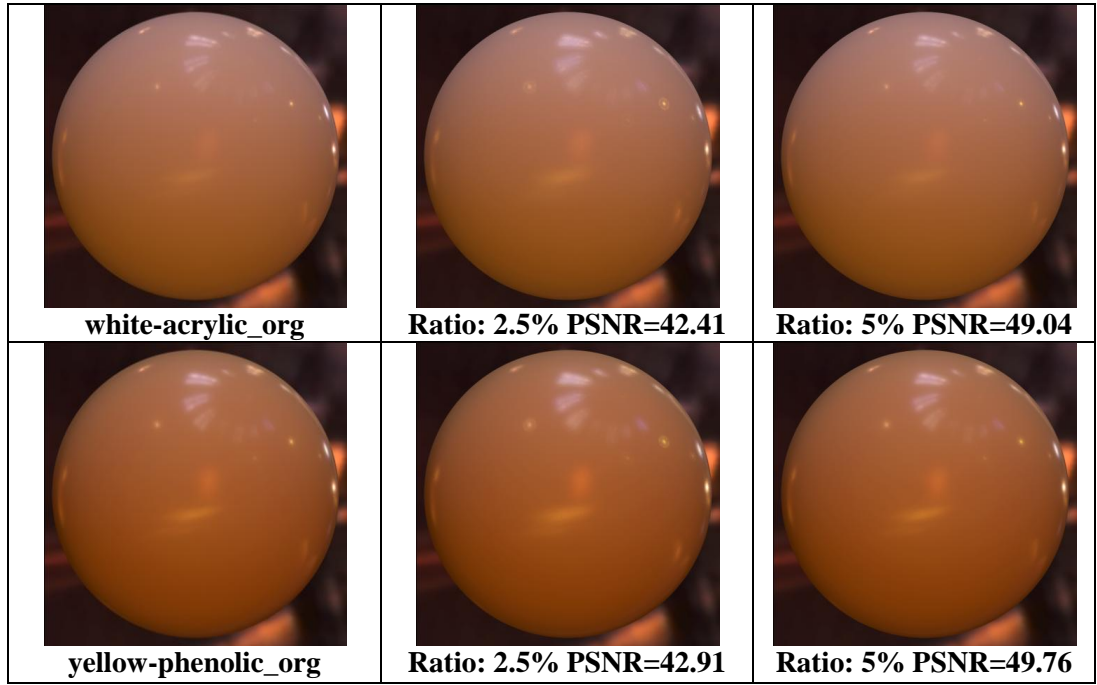
		
delrin_org	Ratio: 2.5% PSNR=44.62	Ratio: 5% PSNR=48.63
		
gold-metallic-paint2_org	Ratio: 2.5% PSNR=39.37	Ratio: 5% PSNR=47.75
		
gray-plastic_org	Ratio: 2.5% PSNR=42.78	Ratio: 5% PSNR=48.77
		
green-acrylic_org	Ratio: 2.5% PSNR=35.45	Ratio: 5% PSNR=41.83

		
green-latex_org	Ratio: 2.5% PSNR=48.86	Ratio: 5% PSNR=51.37
		
green-plastic_org	Ratio: 2.5% PSNR=37.33	Ratio: 5% PSNR=47.22
		
hematite_org	Ratio: 2.5% PSNR=33.90	Ratio: 5% PSNR=45.51
		
ipswich-pine-221_org	Ratio: 2.5% PSNR=46.28	Ratio: 5% PSNR=50.66

 natural-209_org	 Ratio: 2.5% PSNR=45.53	 Ratio: 5% PSNR=49.79
 nickel_org	 Ratio: 2.5% PSNR=37.75	 Ratio: 5% PSNR=47.09
 nylon_org	 Ratio: 2.5% PSNR=41.11	 Ratio: 5% PSNR=45.06
 pearl-paint_org	 Ratio: 2.5% PSNR=47.90	 Ratio: 5% PSNR=51.50

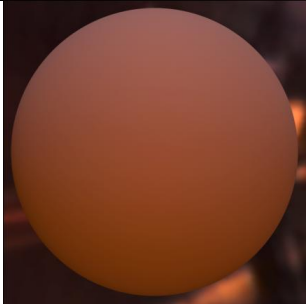
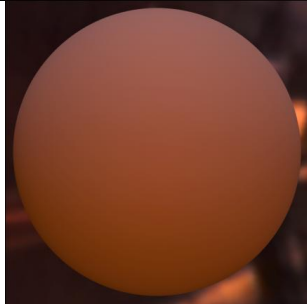
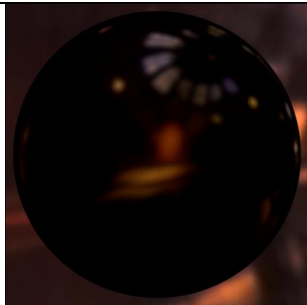
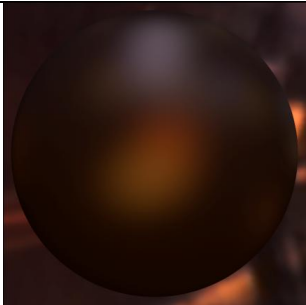
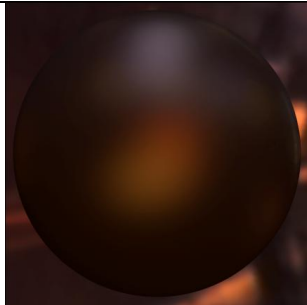
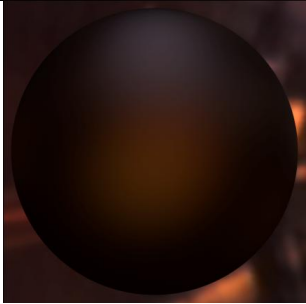
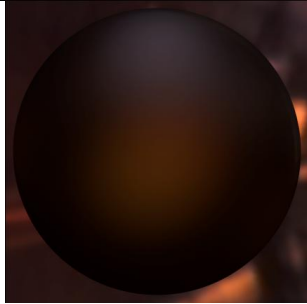
		
pickled-oak-260_org	Ratio: 2.5% PSNR=48.91	Ratio: 5% PSNR=51.58
		
pink-fabric_org	Ratio: 2.5% PSNR=49.53	Ratio: 5% PSNR=51.92
		
pink-jasper_org	Ratio: 2.5% PSNR=41.96	Ratio: 5% PSNR=48.89
		
polyethylene_org	Ratio: 2.5% PSNR=42.81	Ratio: 5% PSNR=46.31

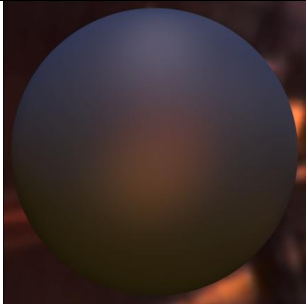
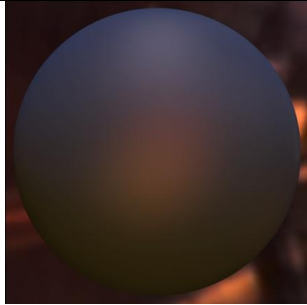
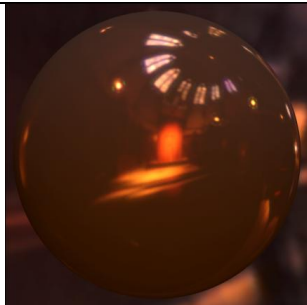
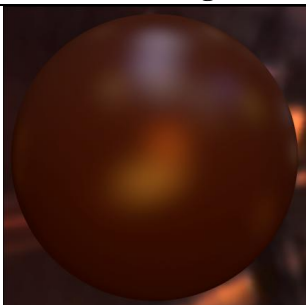
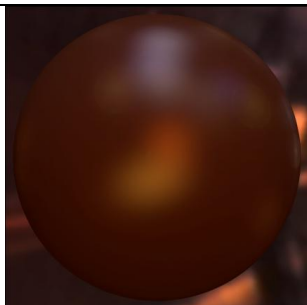
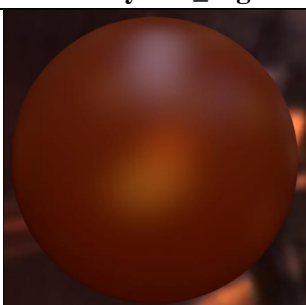
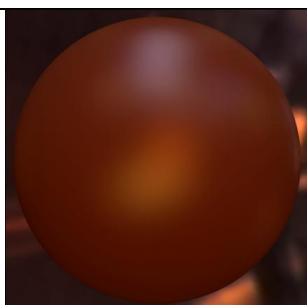
 pure-rubber_org	 Ratio: 2.5% PSNR=49.61	 Ratio: 5% PSNR=51.95
 pvc_org	 Ratio: 2.5% PSNR=41.63	 Ratio: 5% PSNR=48.59
 red-metallic-paint_org	 Ratio: 2.5% PSNR=35.22	 Ratio: 5% PSNR=46.18
 violet-acrylic_org	 Ratio: 2.5% PSNR=37.79	 Ratio: 5% PSNR=47.12

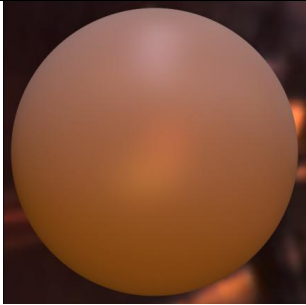
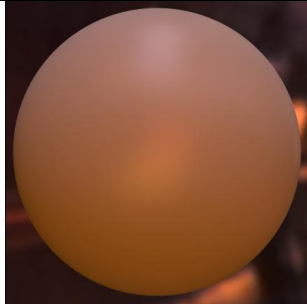
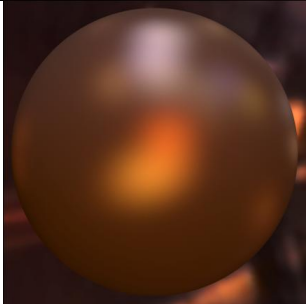
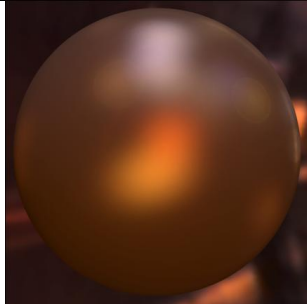
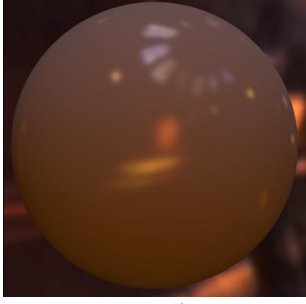
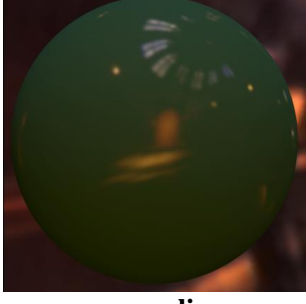


APPENDIX – 5 Results of Reconstruction of BRDF Data Obtained by Ward Model
 Model

		
<p>alum-bronze_org</p>	<p>Ratio: 2.5% PSNR=45.85</p>	
		
<p>alumina-oxide_org</p>	<p>Ratio: 2.5% PSNR=46.83</p>	
		
<p>aluminium_org</p>	<p>Ratio: 2.5% PSNR=40.27</p>	<p>Ratio: 5% PSNR=47.08</p>
		
<p>aventurnine_org</p>	<p>Ratio: 2.5% PSNR=44.41</p>	

		
<p>beige-fabric_org</p>	<p>Ratio: 2.5% PSNR=52.22</p>	
		
<p>black-obsidian_org</p>	<p>Ratio: 2.5% PSNR=45.40</p>	
		
<p>black-oxidized-steel_org</p>	<p>Ratio: 2.5% PSNR=49.71</p>	
		
<p>black-soft-plastic_org</p>	<p>Ratio: 2.5% PSNR=50.93</p>	

		
<p>blue-rubber_org</p>	<p>Ratio: 2.5% PSNR=51.38</p>	
		
<p>brass_org</p>	<p>Ratio: 2.5% PSNR=40.55</p>	<p>Ratio: 5% PSNR=46.97</p>
		
<p>cherry-235_org</p>	<p>Ratio: 2.5% PSNR=48.97</p>	
		
<p>colonial-maple-223_org</p>	<p>Ratio: 2.5% PSNR=49.36</p>	

delrin_org

Ratio: 2.5% PSNR=51.42

gold-metallic-paint2_org

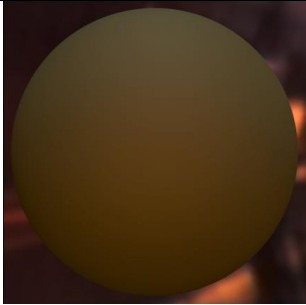
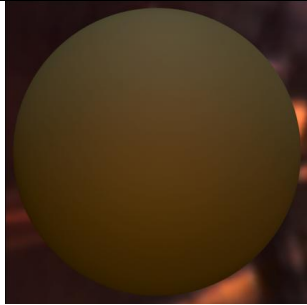
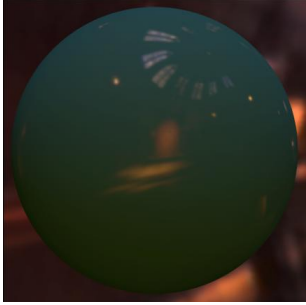
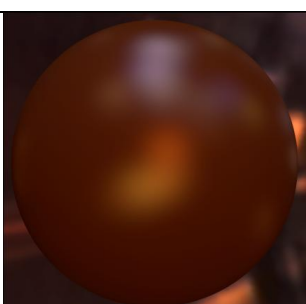
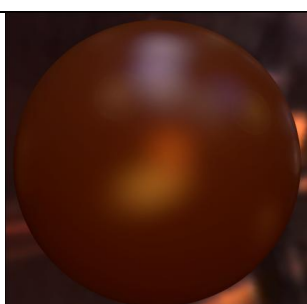
Ratio: 2.5% PSNR=46.10

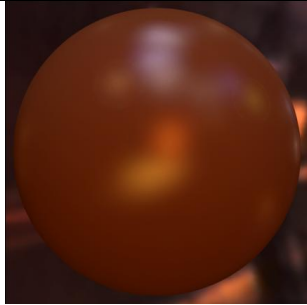
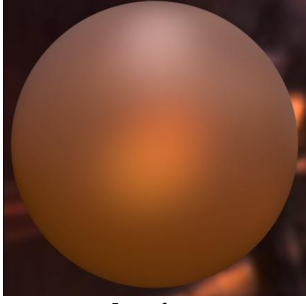
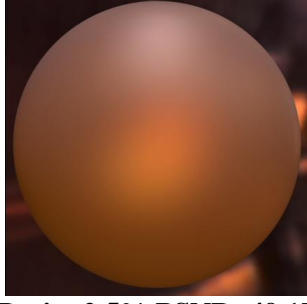
gray-plastic_org

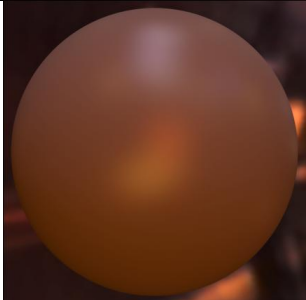
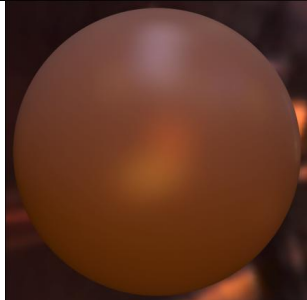
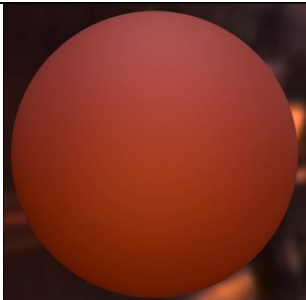
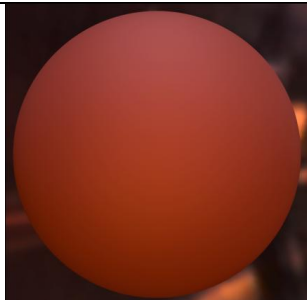
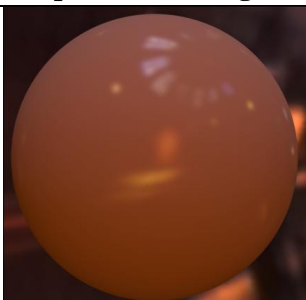
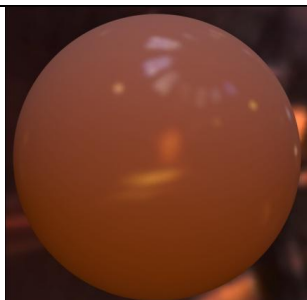
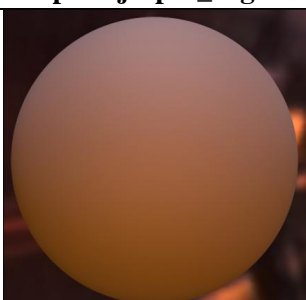
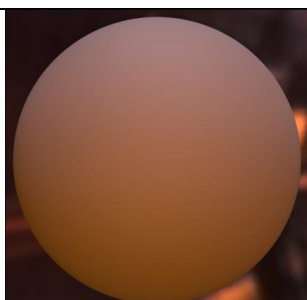
Ratio: 2.5% PSNR=47.71

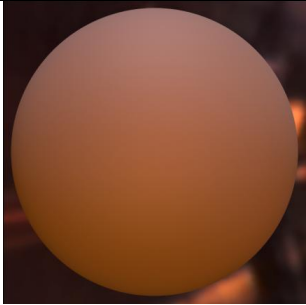
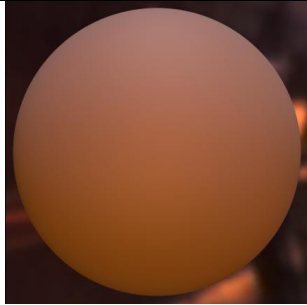
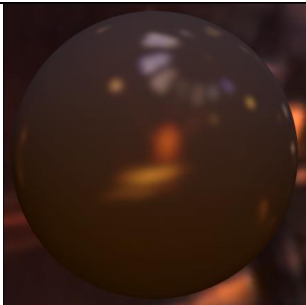
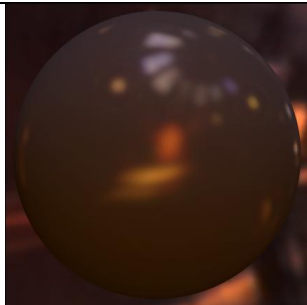
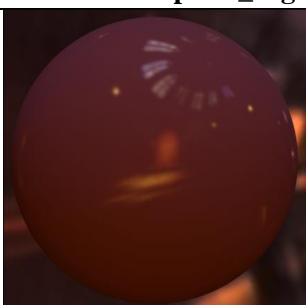
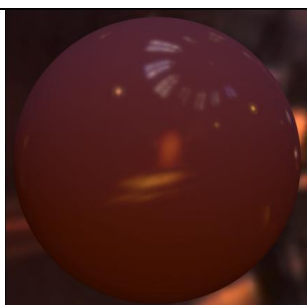
green-acrylic_org

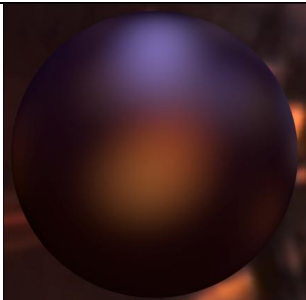
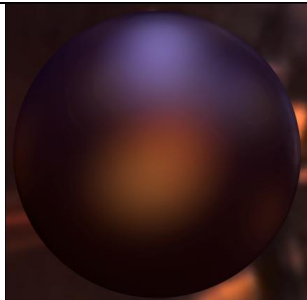
Ratio: 2.5% PSNR=45.64

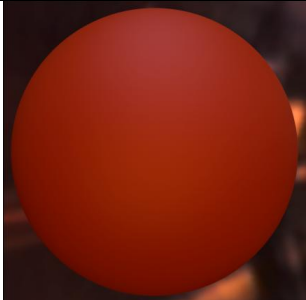
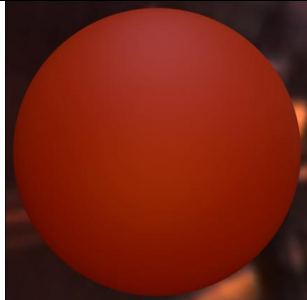
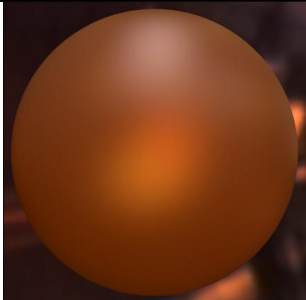
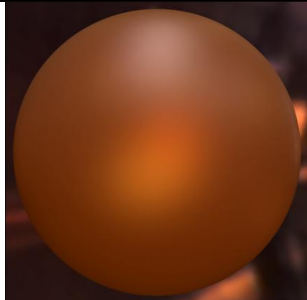
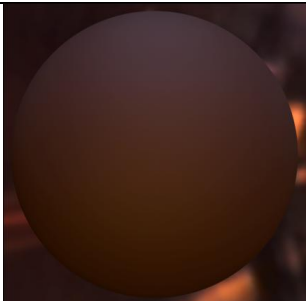
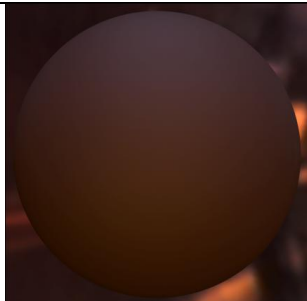
		
<p>green-latex_org</p>	<p>Ratio: 2.5% PSNR=52.18</p>	
		
<p>green-plastic_org</p>	<p>Ratio: 2.5% PSNR=44.44</p>	
		
<p>hematite_org</p>	<p>Ratio: 2.5% PSNR=38.30</p>	<p>Ratio: 5% PSNR=45.62</p>
		
<p>ipswich-pine-221_org</p>	<p>Ratio: 2.5% PSNR=48.28</p>	

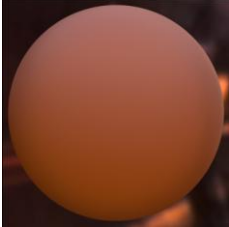
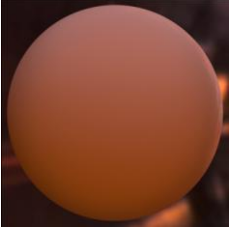
		
<p>natural-209_org</p>	<p>Ratio: 2.5% PSNR=47.17</p>	
		
<p>nickel_org</p>	<p>Ratio: 2.5% PSNR=38.41</p>	<p>Ratio: 5% PSNR=46.65</p>
		
<p>nylon_org</p>	<p>Ratio: 2.5% PSNR=50.74</p>	
		
<p>pearl-paint_org</p>	<p>Ratio: 2.5% PSNR=49.17</p>	

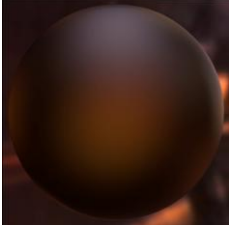
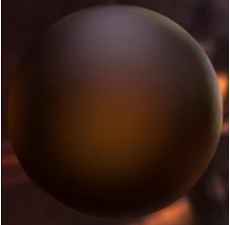
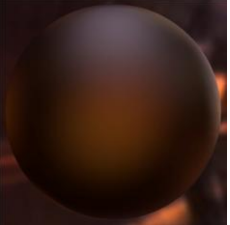
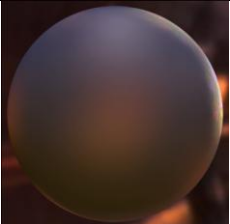
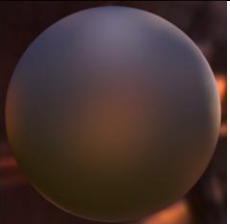
		
<p>pickled-oak-260_org</p>	<p>Ratio: 2.5% PSNR=50.52</p>	
		
<p>pink-fabric_org</p>	<p>Ratio: 2.5% PSNR=50.84</p>	
		
<p>pink-jasper_org</p>	<p>Ratio: 2.5% PSNR=48.26</p>	
		
<p>polyethylene_org</p>	<p>Ratio: 2.5% PSNR=51.50</p>	

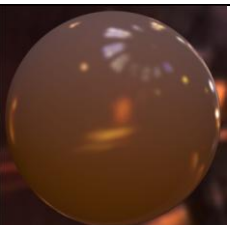
		
<p>pure-rubber_org</p>	<p>Ratio: 2.5% PSNR=51.73</p>	
		
<p>pvc_org</p>	<p>Ratio: 2.5% PSNR=46.80</p>	
		
<p>red-metallic-paint_org</p>	<p>Ratio: 2.5% PSNR=44.03</p>	
		
<p>violet-acrylic_org</p>	<p>Ratio: 2.5% PSNR=46.74</p>	

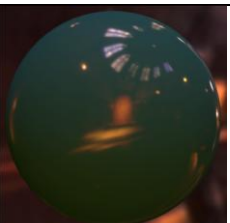
		
<p>white-acrylic_org</p>	<p>Ratio: 2.5% PSNR=49.26</p>	
		
<p>yellow-phenolic_org</p>	<p>Ratio: 2.5% PSNR=47.26</p>	
		
<p>blue-metallic-paint_org</p>	<p>Ratio: 2.5% PSNR=48.60</p>	
		
<p>chrome-steel_org</p>	<p>Ratio: 2.5% PSNR=40.63</p>	<p>Ratio: 5% PSNR=47.26</p>

		
<p>dark-red-paint_org</p>	<p>Ratio: 2.5% PSNR=51.00</p>	
		
<p>fruitwood-241_org</p>	<p>Ratio: 2.5% PSNR=47.11</p>	
		
<p>gold-paint_org</p>	<p>Ratio: 2.5% PSNR=44.86</p>	
		
<p>green-fabric_org</p>	<p>Ratio: 2.5% PSNR=52.07</p>	

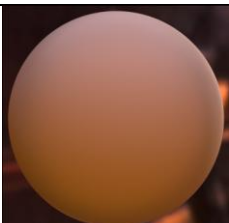
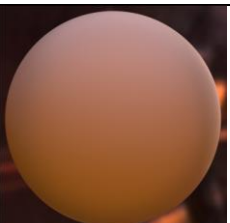
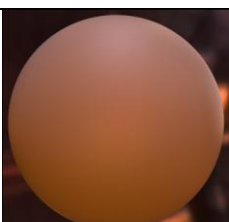
 alum-bronze_org	 Ratio: 2.5% PSNR=33.53	 Ratio: 5% PSNR=39.39	 Ratio: 10% PSNR=43.81
 alumina-oxide_org	 Ratio: 2.5% PSNR=37.93	 Ratio: 5% PSNR=39.39	 Ratio: 10% PSNR=42.71
 aluminium_org	 Ratio: 2.5% PSNR=32.85	 Ratio: 5% PSNR=36.89	 Ratio: 10% PSNR=45.04
 aventurnine_org	 Ratio: 2.5% PSNR=32.37	 Ratio: 5% PSNR=41.96	
 beige-fabric_org	 Ratio: 2.5% PSNR=41.79	 Ratio: 5% PSNR=50.84	

 black-obsidian_org	 Ratio: 2.5% PSNR=32.17	 Ratio: 5% PSNR=44.45	
 black-oxidized-steel_org	 Ratio: 2.5% PSNR=32.76	 Ratio: 5% PSNR=44.46	
 black-soft-plastic_org	 Ratio: 2.5% PSNR=35.84	 Ratio: 5% PSNR=47.53	
 blue-rubber_org	 Ratio: 2.5% PSNR=34.83	 Ratio: 5% PSNR=45.95	
 brass_org	 Ratio: 2.5% PSNR=31.87	 Ratio: 5% PSNR=34.96	 Ratio: 10% PSNR=44.74

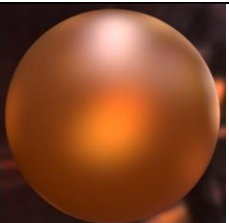
 cherry-235_org	 Ratio: 2.5% PSNR=31.16	 Ratio: 5% PSNR=41.94	
 colonial-maple-223_org	 Ratio: 2.5% PSNR=31.35	 Ratio: 5% PSNR=40.68	
 delrin_org	 Ratio: 2.5% PSNR=34.78	 Ratio: 5% PSNR=44.47	
 gold-metallic-paint2_org	 Ratio: 2.5% PSNR=33.05	 Ratio: 5% PSNR=42.14	
 gray-plastic_org	 Ratio: 2.5% PSNR=32.85	 Ratio: 5% PSNR=42.75	

 green-acrylic_org	 Ratio: 2.5% PSNR=33.70	 Ratio: 5% PSNR=40.10	
 green-latex_org	 Ratio: 2.5% PSNR=42.29	 Ratio: 5% PSNR=50.53	
 green-plastic_org	 Ratio: 2.5% PSNR=36.98	 Ratio: 5% PSNR=39.87	 Ratio: 10% PSNR=44.51
 hematite_org	 Ratio: 2.5% PSNR=30.54	 Ratio: 5% PSNR=33.74	 Ratio: 10% PSNR=45.35
 ipswich-pine-221_org	 Ratio: 2.5% PSNR=30.12	 Ratio: 5% PSNR=41.19	

 natural-209_org	 Ratio: 2.5% PSNR=30.92	 Ratio: 5% PSNR=40.77	
 nickel_org	 Ratio: 2.5% PSNR=32.12	 Ratio: 5% PSNR=38.12	 Ratio: 10% PSNR=44.98
 nylon_org	 Ratio: 2.5% PSNR=35.00	 Ratio: 5% PSNR=42.16	
 pearl-paint_org	 Ratio: 2.5% PSNR=45.96	 Ratio: 5% PSNR=36.50	
 pickled-oak-260_org	 Ratio: 2.5% PSNR=38.93	 Ratio: 5% PSNR=46.12	

 pink-fabric_org	 Ratio: 2.5% PSNR=42.22	 Ratio: 5% PSNR=49.23	
 pink-jasper_org	 Ratio: 2.5% PSNR=34.58	 Ratio: 5% PSNR=42.76	
 polyethylene_org	 Ratio: 2.5% PSNR=39.62	 Ratio: 5% PSNR=49.04	
 pure-rubber_org	 Ratio: 2.5% PSNR=38.77	 Ratio: 5% PSNR=48.64	
 pvc_org	 Ratio: 2.5% PSNR=32.52	 Ratio: 5% PSNR=32.52	 Ratio: 10% PSNR=44.46

 red-metallic-paint_org	 Ratio: 2.5% PSNR=33.98	 Ratio: 5% PSNR=42.67	
 violet-acrylic_org	 Ratio: 2.5% PSNR=33.25	 Ratio: 5% PSNR=42.48	
 white-acrylic_org	 Ratio: 2.5% PSNR=35.55	 Ratio: 5% PSNR=40.97	
 yellow-phenolic_org	 Ratio: 2.5% PSNR=34.33	 Ratio: 5% PSNR=43.80	
 blue-metallic-paint_org	 Ratio: 2.5% PSNR=34.51	 Ratio: 5% PSNR=46.00	

 chrome-steel_org	 Ratio: 2.5% PSNR=32.10	 Ratio: 5% PSNR=36.58	 Ratio: 10% PSNR=45.43
 dark-red-paint_org	 Ratio: 2.5% PSNR=38.28	 Ratio: 5% PSNR=47.41	
 fruitwood-241_org	 Ratio: 2.5% PSNR=30.46	 Ratio: 5% PSNR=41.93	
 gold-paint_org	 Ratio: 2.5% PSNR=35.53	 Ratio: 5% PSNR=44.68	
 green-fabric_org	 Ratio: 2.5% PSNR=36.89	 Ratio: 5% PSNR=49.39	

CURRICULUM VITEA

Nurcan Seylan was born in 1970, Izmir – Turkey. She has a BSc degree from Ege University, Computer Engineering, after graduating in 1992. Then she worked as a software developer between years 1992-2000. She has been working as lecturer at Ege University, Vocational High School, Computer Programming program, since 2002. She graduated from Ege University, International Computer Institute with a MSc degree in 2008. She started her doctorate education at Yaşar University in 2009.